

We are IntechOpen, the world's leading publisher of Open Access books Built by scientists, for scientists

6,300

Open access books available

171,000

International authors and editors

190M

Downloads

Our authors are among the

154

Countries delivered to

TOP 1%

most cited scientists

12.2%

Contributors from top 500 universities



WEB OF SCIENCE™

Selection of our books indexed in the Book Citation Index
in Web of Science™ Core Collection (BKCI)

Interested in publishing with us?
Contact book.department@intechopen.com

Numbers displayed above are based on latest data collected.
For more information visit www.intechopen.com



Fabrication and Sensing Applications of Special Microstructured Optical Fibers

Zhengyong Liu and Hwa-Yaw Tam

Additional information is available at the end of the chapter

<http://dx.doi.org/10.5772/intechopen.70755>

Abstract

This chapter presents the fabrication of the special microstructured optical fibers (MOFs) and the development of sensing applications based on the fabricated fibers. Particularly, several types of MOFs including birefringent and photosensitive fibers will be introduced. To fabricate the special MOFs, the stack-and-draw technique is employed to introduce asymmetrical stress distribution in the fibers. The microstructure of MOFs includes conventional hexagonal assemblies, large-air hole structures, as well as suspended microfibers. The birefringence of MOFs can reach up to 10^{-2} by designing the air hole structure properly. Fiber Bragg gratings as well as Sagnac interferometers are developed based on the fabricated special MOFs to conduct sensing measurement. Various sensing applications based on MOFs are introduced.

Keywords: microstructured optical fibers, MOFs, fiber sensor, interferometry, FBG

1. Introduction

Microstructured optical fibers (MOFs), which have air-hole structure along the fiber length, have attracted tremendous attention in the development of novel fiber sensors for a multitude of industry applications. Majority of the effort has been focused on silica photonic crystal fibers (PCFs), which are composed of many air channels arranged in hexagonal (honeycomb) shape [1–3]. Since Phillip St. Russel proposed the use of silica/air structure to design the fiber and realized all-silica single mode PCF in 1990s [4, 5], significant advances were made in supercontinuum generation [6–8], fiber lasers [9–11], as well as fiber-optic sensor [12–14]. More flexible fiber design and different kinds of materials are used in MOFs, for example, using tellurite or chalcogenide glass rather than pure silica glass [7] and suspended-core structure instead of honeycomb arrangement [13]. Light is guided in PCFs by two principles, namely, the modified total internal

reflection (M-TIR) and the photonic bandgap (PBG). Typically, fibers employing the M-TIR principle have a solid core made of pure silica or silica doped with metal ions (e.g., Ge, Er, Yb, Tm, Co), whereas PCFs using the PBG principle have hollow core. Even though the fiber core is free of dopants or hollow, light can be confined in the core by cladding with periodic air-hole structure due to the lower effective refractive index of cladding or the bandgap effect. The air-hole structure or dopants of MOFs modified the mechanical and optical properties of the fibers, and thus, the MOFs can be tailored to suit specific sensor requirements.

Physical parameters, such as strain, temperature, pressure, vibration, torsion, etc., have been measured accurately using PCF-based sensors [15, 16]. Basically, the air-hole structure in MOFs for sensing applications is designed to give the desired stress distribution in the fiber so that the stress is enhanced by any external physical perturbation to the fiber, leading to change of the effective index of the guided mode in the core. The stress change can be induced either thermally or mechanically such as pulling, compression, and twist. Various kinds of sensors can be implemented using such approach. For instance, polarization-maintaining PCFs with an asymmetrical stress distribution provide an excellent option to construct Sagnac interferometer for the measurement of oil pressure with very high sensitivity of 3.4 nm/MPa [17]. On the other hand, the core in hollow-core PCFs can be filled with gas or analytes to enhance the interaction between the materials in the hollow core and light to realize highly sensitive gas and chemical sensors [18–20]. Alternatively, the air channels in the cladding of index-guiding PCFs confining light via the M-TIR principle can be filled with the materials to be sensed. The materials in the air holes change the index or stress distribution in the cladding and modify the guided light in the core [21–23]. By selectively filling liquid into some of the air holes, refractive index sensor with extremely high sensitivity = 12,750 nm/RIU was reported [23]. The ease and flexibility of fabricating MOFs with different structures bring tremendous opportunities in the development of fiber-optic sensors suited for a wide range of applications.

In this chapter, we present the fabrication techniques of some special MOFs and demonstrate the sensing applications based on the fabricated fibers. The stack-and-draw approach is used to make the fibers; however, specific modifications were introduced to obtain different air-hole structures, especially to induce the asymmetrical stress distribution in the fiber to realize highly sensitive pressure sensors. Various kinds of MOFs including twin-core PCF, high birefringence PCF, suspended core fiber, suspended microfiber, as well as two semicircle holes fiber were fabricated for sensing applications. MOF-based pressure sensors were fabricated using fiber Bragg grating (FBG) and/or interferometry technique. Section 2 will present the fabrication techniques used to fabricate our special MOFs. Section 3 describes the use of MOF sensors for the oil and gas industry. The summary is given at the end of this chapter.

2. Fabrication and characterization of special microstructured optical fibers

2.1. Fabrication of MOFs

Several approaches are being used to fabricate MOFs, including extrusion [24], casting/molding [25], mechanical drilling [26], and stack-and-draw [27]. The stack-and-draw technique is

the most versatile and flexible. This is because by stacking small capillaries, not only various structures can be implemented but also different materials besides silica glass can be utilized. Extrusion, casting, and drilling are widely used to make polymer or soft-glass MOFs due to the much lower softening temperature of these materials. In contrast, it is easier to stack different structures regardless of materials. In addition to fabricate conventional hexagonal air-hole structures, more complicated superlattice structures can be fabricated using circular capillaries that are arranged in patterns to approximate triangular holes, square holes, and elliptic holes [27, 28]. We demonstrated the fabrication of superlattice PCFs using the stack-and-draw technique [27] to realize elliptical holes in the cladding and its optical characteristics are comparable to the design with ideal elliptical holes. Various designs of MOFs with either side hole, two core, or suspended core were used to fabricate optical fiber sensors for different sensing applications. Some of the circular capillaries arranged in hexagonal pattern can be replaced by capillaries/rods of different diameters. The stack-and-draw method offers the flexibility to fabricate a large variety of MOF sensors suited for different industries.

Figure 1 illustrates the process of fabricating a twin-core PCF (TC-PCF) using the stack-and-draw technique. Hexagonal structure is the natural pattern when stacking circular capillaries of equal diameter together. Typically, pure silica capillaries and rods are first drawn before the stacking process. To fabricate PCFs with n -layer of air hole in hexagonal pattern, $3n(n+1)$ of capillaries plus one rod for the central core are required. The stacked assemble can be secured using tungsten wire and then fixed in position by melting some of the capillaries. Alternatively, the entire assemble can be directly stacked inside a jacket tube, and the gaps are filled with silica rods of various outer diameters.

Basically, two drawing stages are employed to fabricate MOFs, particularly for complicated structures that have many layers of air holes. The first drawing stage is to draw the stacked assembly into cane with the desired outer diameter of 1–2 mm, as illustrated in **Figure 1(c)**. The

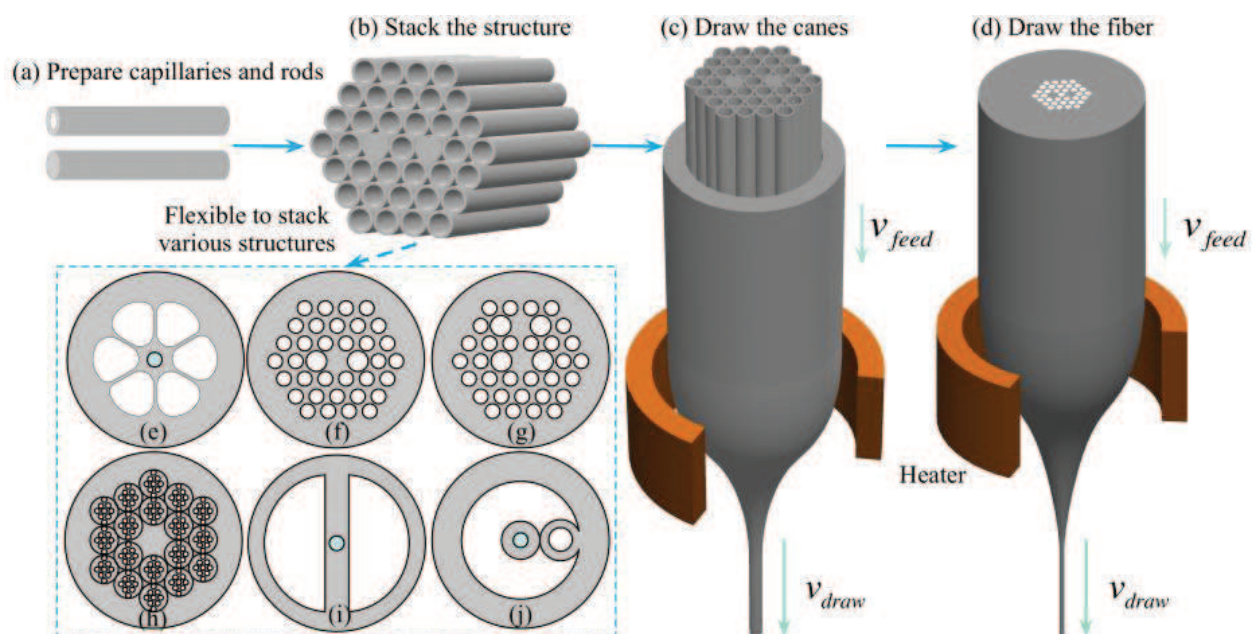


Figure 1. Illustration of the stack-and-draw method used in microstructured optical fibers (MOFs) fabrication.

cane is then inserted into a jacket tube, forming a second preform. The final fiber is drawn from the second preform, as shown in **Figure 1(d)**. By using two drawing stages, the total reduction ratio of diameter can be divided into two parts. Using smaller reduction ratio during the first drawing stage, the stacked assemble can be drawn with minimal distortion from the desired structure. For simple structures or structures with only a few large air holes, one drawing stage is normally adequate. For the superlattice structure reported in Ref. [27], three drawing stages were used, where the first drawn cane was used to make a second stack. To draw the MOFs properly, the drawing temperature $\approx 1900^\circ\text{C}$ is lower than that of pulling all silica single mode fiber (SMF). The air hole would collapse if the drawing temperature is too high [29]. The collapse ratio is inversely proportional to the viscosity and the ratio of drawing velocity over feeding velocity (i.e., $v_{\text{draw}}/v_{\text{feed}}$). High temperature leads to low viscosity and ultimately large collapse ratio. Collapse ratio equal to 1 means air holes completely collapse. Relatively fast drawing velocity is preferable to maintain a certain tension to sustain the air-hole structure. However, large tension also results in poor fiber strength, which makes the fiber fragile. Thus, there is a trade-off to adjust the drawing temperature and tension. The control of tension and temperature is particularly important for drawing MOFs with large air holes.

Figure 2 shows the scanning electronic microscopic (SEM) photos of the cross-section of some fabricated MOFs in our lab using the stack-and-draw technique. By introducing air holes with different diameters, the mechanical properties of the fiber can be modified. In particular, the noncircularly symmetrical air-hole structure provides some degree of tailoring the stress

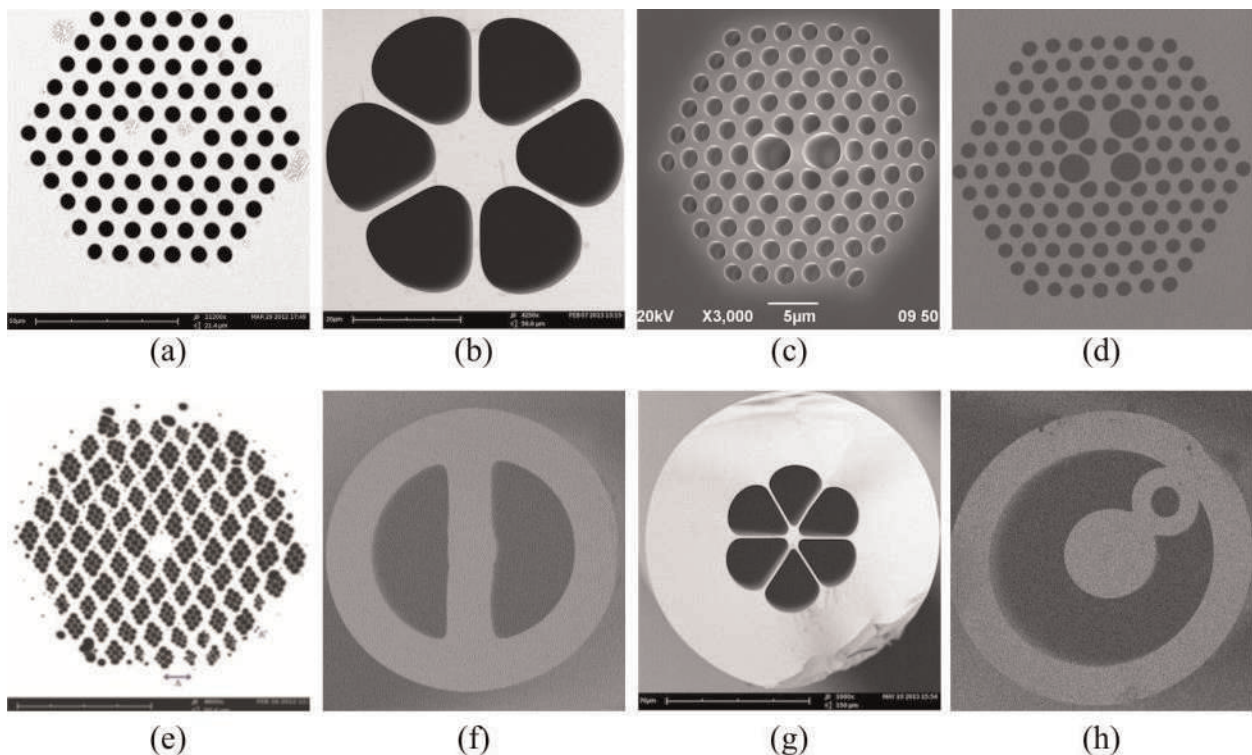


Figure 2. Scanning electronic microscopic photos of the cross section of the fabricated MOFs by using various stacking strategies. The examples shown are (a) twin-core photonic crystal fiber (TC-PCF) [12], (b) six-hole suspended-core fiber (SH-SCF), (c) high birefringence PCF (HB-PCF), (d) two-core HB-PCF, (e) superlattice PCF [27], (f) two semicircle hole fiber, (g) high birefringence suspended-core fiber (HB-SCF) [13], and (h) single-ring suspended fiber [30].

distribution in the fiber. Basically, the stress distribution of circularly symmetrical structures, including the standard single-mode optical fiber, is identical along the two polarization axes. MOFs with noncircularly symmetrical cross-section are birefringent. **Figure 2(a)** shows a two-core MOF, where the optical coupling between the cores is affected by pressure. **Figure 2(b)** shows a 6-hole MOF for the measurement of refractive-index changes of fluid. The cores of the MOFs shown in **Figure 2(c)–(g)** are elliptical, and the fibers are highly birefringent. **Figure 2(h)** shows a small-diameter fiber suspended inside a fiber and is designed for vibration measurement.

2.2. Twin-core photonic crystal fiber

A twin-core PCF was developed as an alternative sensor to standard single-mode optical fiber for pressure measurement. The air-hole structure of the TC-PCF is shown in **Figure 2(a)**, where two capillaries are replaced by two pure silica rods in the stacked assembly. The fabrication process is described schematically in **Figure 1**, and details can be found in Ref. [12]. The fiber was drawn at a temperature close to 1900 C. The outer diameter of the fiber is 125 μm , and diameter of two cores is $\sim 2.5 \mu\text{m}$. The hole diameter is $\sim 1.1 \mu\text{m}$, and pitch is $\sim 1.85 \mu\text{m}$. As the distance between the two cores is so close ($\sim 4 \mu\text{m}$), the coupling effect between each other is strong. The modes guided in each core are combined and known as supermodes, i.e., even and odd modes [12, 31, 32]. Particularly in the fabricated TC-PCF, there are x -polarized even and odd modes and y -polarized even and odd modes. **Figure 3** shows the simulated mode profile of these modes.

According to the coupling theory, the coupling length of even and odd modes at each polarization (e.g. x polarization) can be written as

$$L_c(\lambda) = \frac{\lambda}{2|n_{p,x\text{-even}} - n_{p,x\text{-odd}}|} = \frac{\lambda}{2|\Delta n_{x,p}|}, \quad (1)$$

where $n_{p,x\text{-even}}$ and $n_{p,x\text{-odd}}$ represent the phase effective index of the x -polarized even and odd modes respectively, and $\Delta n_{p,x}$ stands for their difference. The effective index of each mode changes with the stress distribution induced by the external environment (such as pressure and strain), which eventually causes the corresponding change of coupling coefficient. As for

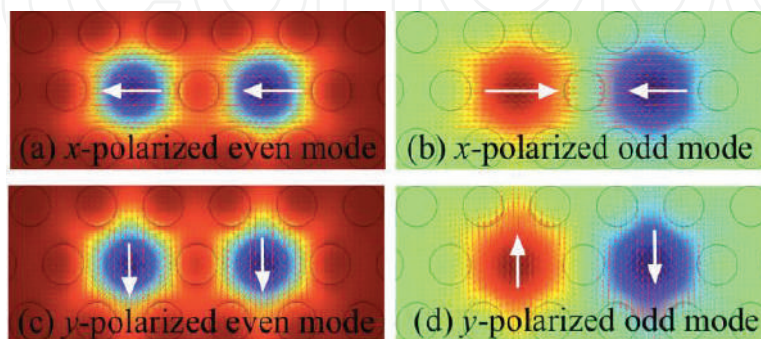


Figure 3. Simulated profiles of the electrical field for the x -polarized even and odd modes and y -polarized even and odd modes supported in TC-PCF, where the arrows show the direction of the field (adapted from ref. [12], OSA).

one polarization direction, the power coupled from one core to the other after propagating a distance of L can be expressed as

$$I_x(\lambda) = \sin^2 \left[\frac{\pi}{2L_c(\lambda)} L \right] = \sin^2 \left(\frac{\pi}{\lambda} \Delta n_{x,p} L \right). \quad (2)$$

Since the x and y polarization are orthogonal, the total output power of the transmission is the sum of both polarizations, which is then expressed as

$$I(\lambda) = I_x(\lambda) + I_y(\lambda) = 1 - \cos \left[\frac{\pi}{\lambda} (\Delta n_{x,p} + \Delta n_{y,p}) L \right] \cdot \cos \left[\frac{\pi}{\lambda} (\Delta n_{x,p} - \Delta n_{y,p}) L \right]. \quad (3)$$

It can be seen that the transmission spectrum of the TC-PCF is modulated due to the mutual influence of the two polarizations. If considering a short wavelength range, the fringe spacing can be approximated as

$$\Delta\lambda = \frac{2\lambda^2}{(\Delta n_{x,g} + \Delta n_{y,g})L}. \quad (4)$$

Here, $\Delta n_{x,g}$ and $\Delta n_{y,g}$ are the group effective index difference of the even and odd modes of x - and y -polarizations, respectively. The group index (n_g) and phase index (n_p) have a relationship of $n_g = n_p - \lambda dn_p/d\lambda$. The calculated $\Delta n_{x,g}$ and $\Delta n_{y,g}$ are 3.745×10^{-3} and 3.386×10^{-3} , respectively. The calculated fringe spacing for a 110-cm long TC-PCF is ~ 0.613 nm. In experiment, the TC-PCF was spliced to two SMFs using manual splicing mode [33, 34]. A broadband source (BBS) and optical spectrum analyzer (OSA) were utilized to monitor the transmission spectrum of the output. To obtain high fringe contrast, an offset in the alignment and repeated arc discharges are needed. **Figure 4** shows the calculated and experimental transmission spectrum. Both results show modulation on the interference. Besides, the fringe spacing obtained experimentally is about 0.676 nm, which is also in good agreement with the calculated value. The obtained transmission spectrum of TC-PCF is sensitive to external physical perturbation and can be employed as pressure sensors.

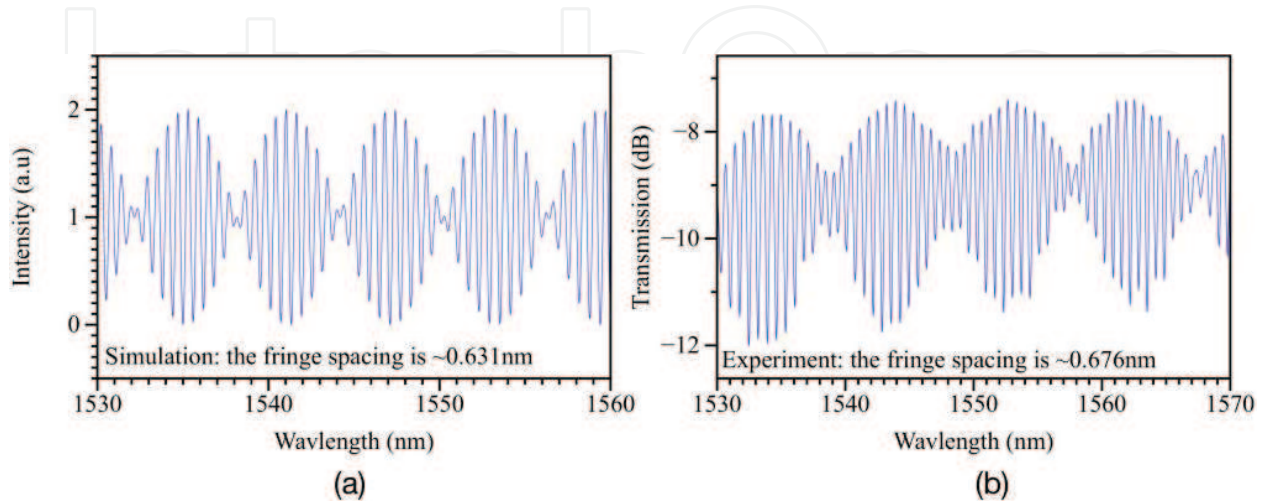


Figure 4. (a) Simulated and (b) experimental transmission spectra of a 110-cm long TC-PCF, adapted from ref. [12], OSA.

2.3. High birefringence microstructured optical fiber

In addition to the multiple cores achieved by replacing certain capillaries during stacking, capillaries with different inner diameters can be used to fabricate noncircularly symmetric air-hole structures to introduce birefringence in MOFs. The effective index of the x -polarized mode and y -polarized mode is different in birefringent MOFs. The birefringence of the fiber is defined as the index difference of the two polarization modes (i.e., $B = |n_x - n_y|$). In optical fiber communications, birefringent fiber is utilized to realize polarization maintaining. Commonly used polarization-maintaining fibers (PMFs) have a bowtie, elliptical, or PANDA structures [35]. The main feature of these fibers is that there are two heavily doped parts in the cladding, e.g., PANDA fiber [36] or an elliptical core designed to induce noncircularly symmetric stress to the core. The stress applying part in the cladding or the asymmetrical geometry of the fiber is regarded as exterior stress to the fiber core, whereas the thermal expansion of the noncircularly symmetric core yields interior stress to the core. The total birefringence of the fiber is composed of the contributions from exterior stress, interior stress, or both, depending on the fiber type.

Similar concept is employed in MOFs. Unlike conventional PMFs, high birefringence MOFs (HB-MOFs) exhibit the flexibility of modifying the fiber geometry and inducing exterior stress to the core. MOF fabrication permits the ease of introducing various air-hole structures in the cladding and breaks the circular symmetry of the fiber. Birefringence is an important property in fiber sensors for the measurement of many physical parameters. PM-PCF has been demonstrated to be a good candidate in the measurements of pressure [17], strain [37], temperature [38], torsion [39], etc. Most of these applications are based on the commercially available PM-PCF from NKT Photonics (PM-1550-01), which has a birefringence of $\sim 4 \times 10^{-4}$ at the wavelength of ~ 1550 nm.

The birefringence of MOFs allows for the construction of Sagnac interferometer (SI) by simply splicing PM-PCF between two output ports of a 3-dB coupler. The 3-dB coupler splits the light from one input port into two counter-propagating beams that interfere with each other at the 3-dB coupler after propagating through the PM-PCF, as shown in **Figure 5(a)**. The phase difference (ϕ) of the two polarization is $2\pi BL/\lambda$, where B and L are the birefringence and length of the fiber, respectively. At the valleys of the spectrum, the phase difference is always equal to $2k\pi$ (k is an integer). As for two adjacent valleys, the change of phase difference is 2π and equals $(d\phi/d\lambda) \cdot \Delta\lambda$, where $\Delta\lambda$ is the wavelength difference of these two adjacent valleys. Thus, the birefringence of one HB-MOF can be expressed by

$$G = \frac{\lambda_1 \cdot \lambda_2}{\Delta\lambda \cdot L}, \quad (5)$$

where λ_1 and λ_2 represents the two adjacent valley wavelengths and G is the group birefringence, which can be measured via the experimental SI spectrum. **Figure 5(b)** plots the spectrum of a typical SI constructed using in-house HB-PCF (shown in **Figure 2(c)**) having a length of 5.5 cm. The wavelengths of two valleys close to 1550 nm are 1547.16 nm and 1550.66 nm. The group birefringence of this fiber is calculated to be $\sim 1.25 \times 10^{-2}$.

The birefringence of the MOFs offers an alternative to conventional PMFs in the construction of interferometric sensors using phase difference of two polarization modes propagating in the

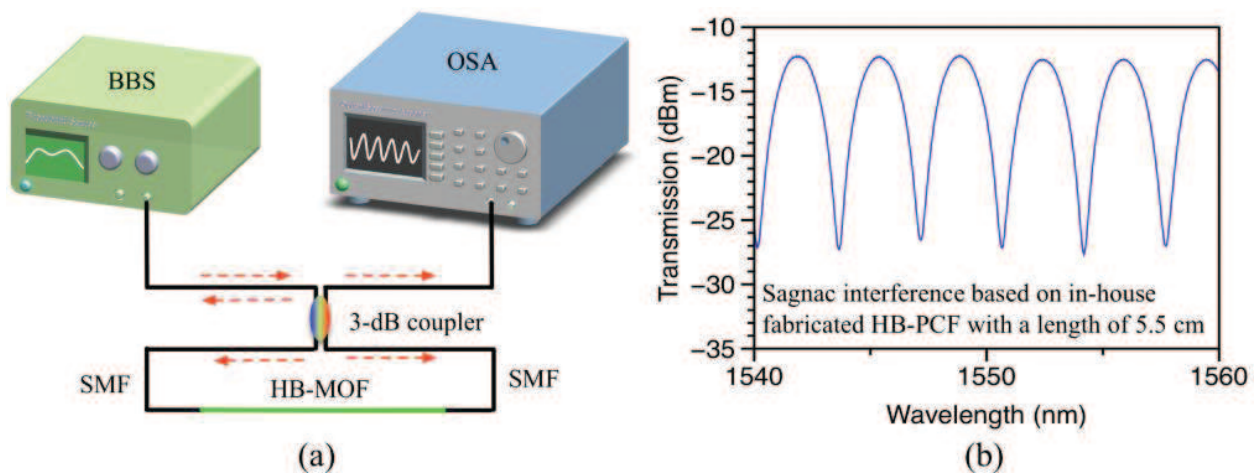


Figure 5. (a) Schematic figure of the configuration of a typical Sagnac interferometer realized by HB-MOF and (b) interference spectrum of a SI based on a 5.5-cm long in-house fabricated HB-PCF.

MOFs. The sensitivity of interferometric sensors is highly dependent on the birefringence change induced by external perturbations. Therefore, the arrangement of the air-hole structure that transfers the external perturbation to the optical mode in the core is important. We designed and fabricated several types of MOFs to measure oil pressure and refractive index of fluid for biomedical sensing. The sensitivity of the sensors varies greatly with the geometry of the core and cladding, as well as the sensing principle employed in the sensors. In general, interferometry-based sensors exhibit better sensitivity than grating-based sensors. However, in interferometry-based sensors, the sensing information is encoded in the spectral dips/peaks, which is much broader than the reflection peaks of grating-based sensors. Detecting the shift of the dips/peaks of a broad spectrum accurately is more difficult, therefore could affect the measurement accuracy. The sensing performance of different MOFs will be presented and compared in the following two sections.

Figure 2(c)–(g) show the SEM photos of some of the MOFs with high birefringence fabricated in our lab. As the air-hole structure is different, the birefringence of the fibers is not the same. The phase and group birefringence of HB-PCF we fabricated (show in **Figure 2(c)**) are measured to be 1.1×10^{-2} and 1.25×10^{-2} . Both values are in good agreement with the calculated values of 1.4×10^{-2} using finite element method. The two large holes in the cross section of the fiber shown in **Figure 2(c)** are slightly elongated, resulting in the desired noncircularly symmetric air-hole structure for high birefringent fiber. For index-guiding MOFs made of silica, this fiber possesses the highest birefringence in reported literatures. **Table 1** lists the comparison of our various HB-MOFs and others reported in the literatures.

Basically, elliptical core leads to higher birefringence because the two polarization modes are along with the major and minor axis of the elliptical core, individually. Due to the feature that optical mode is confined in the air for hollow-core PCF, even slight imperfection can influence the light propagation significantly, such as the loss and modal profile. Thus, hollow-core PCF with elliptical core exhibits very high birefringence even for small ellipticity. For example, the elliptical core with an aspect ratio of 1.16 exhibits a group birefringence of 2.5×10^{-2} [52]. MOFs

PM fiber type	Description of the structure	Reported date	Measured birefringence
HB PM-PCF, Figure 2(c)	Two large holes close to an elliptical core	May, 2013 [40]	1.25×10^{-2}
Superlattice PCF, Figure 2(e)	Superlattice with rhombic cell of 9 holes	June, 2014 [27]	8.5×10^{-4}
6-hole suspended-core fiber, Figure 2(g)	Elliptical core suspended by 6 large air holes	June, 2014 [13]	5×10^{-4}
Semicircle hole fiber, Figure 2(f)	Two large semicircle side holes	August, 2017	1×10^{-4}
Low-loss PM-PCF	Two large air holes close to the core	December, 2011 [41]	1.4×10^{-3}
PANDA PMF	Stress-applying parts with PANDA shape	July, 1981 [42]	8.5×10^{-5}
Bow-tie PMF	Stress-applying parts with bow-tie shape	November, 1982 [43]	4.87×10^{-4}
First fabricated HB PCF	Twofold rotational symmetry	September, 2000 [44]	3.85×10^{-3}
Side-hole fiber	Two side holes with elliptical Ge-core	September, 2008 [45]	1.39×10^{-4}
HB MOF	Irregular air holes with elliptical core	July, 2007 [46]	1.1×10^{-2}
Butterfly-type MOF	Twofold air-hole structure with butterfly shape	June, 2010 [47]	1.8×10^{-3}
Squeezed lattice PCF	Squeezed air holes with two big holes	February, 2010 [48]	5.5×10^{-3}
HB index-guiding PCF	Elliptical core by achieved by replacing two holes	June, 2001 [49]	9.3×10^{-4}
Fiberized glass ridge waveguide	Borosilicate glass-based fiberized ridge waveguide	April, 2015 [50]	9.5×10^{-3}
HB nonlinear MOF	Small elliptical core	July, 2004 [51]	7×10^{-3}
Hollow-core PBGF	Elliptical hollow core	August, 2004 [52]	2.5×10^{-2}
SF57 glass MOF at 1.06 μm wavelength	Asymmetric structure with elliptical air holes	May, 2017 [53]	9×10^{-2}
Chalcogenide glass PCF at 7.5 μm wavelength	Two large air holes close to the core	April, 2016 [54]	1.5×10^{-3}

Table 1. Comparison of birefringent MOFs reported in the literatures.

made of other type of glass (e.g. SF57, Chalcogenide glass) also have large birefringence in the order of 10^{-2} , if the structure is optimized. Sensors with high birefringence allow the implementation of compact sensing configuration because shorter fiber can be used. The sensing information of Sagnac interferometer is encoded in the wavelength shift of the interference spectrum. The phase difference at one valley is equal to $2k\pi$, and the sensitivity, which is defined as the wavelength shift per unit change in the measurand, can be expressed by

$$\frac{d\lambda}{dX} = \frac{\lambda}{G} \frac{\partial B}{\partial X}, \quad (6)$$

where X is the measurand, such as pressure, temperature, refractive index, etc., B is the modal (phase) birefringence, and $\frac{\partial B}{\partial X}$ is the polarimetric sensitivity. Note that the length effect is neglected in Eq. (6), which is not applied to the strain measurement. The strain is mainly

caused by elongation and thus needs to be taken into account to estimate the sensitivity, which can be formulated by considering the length, and the equation becomes

$$\frac{d\lambda}{d\varepsilon} = \frac{\lambda \cdot [\partial B_1(\lambda, \varepsilon)/\partial \varepsilon + B_1(\lambda, \varepsilon)]}{G_1(\lambda, \varepsilon) + (1/\alpha - 1) \cdot G_2(\lambda)}, \quad (7)$$

where $B_1(\lambda, \varepsilon)$ and $G_1(\lambda, \varepsilon)$ are the phase and group modal birefringence for the MOF section under stressed, $G_2(\lambda)$ is the group modal birefringence for the MOF section without strain applied, and α is the ratio of fiber section under strain over total length of the MOF. Different air-hole structures give different values of birefringence derivative with respect to the measurands; therefore, it is important to design the MOFs with the desirable birefringence derivative to optimize the sensing performance. In terms of the form of wavelength shift, the sensitivity is inversely proportional to the birefringence. The key consideration to achieve high sensitivity is to have large-phase birefringence change with measurands but relatively low-group birefringence.

2.4. Sensors based on fiber Bragg grating inscribed in MOFs

The ease and flexibility of fabrication of birefringent MOFs result in the increasing use of these fibers in Sagnac interferometric sensors. Fiber Bragg gratings can be inscribed in MOFs to increase their sensing capabilities. However, it is more difficult to inscribe FBGs in the MOFs compare to SMFs due to the existence of the air holes that diffract the UV light needed to write gratings. UV light at 193, 248, 213, and 266 nm, as well as femtosecond laser [55–57], is being used to inscribe FBGs in various types of MOFs. 193 nm lasers [56] and femtosecond lasers were used to write FBGs in nonphotosensitive MOFs. These lasers induced physical deformation in the fiber cores. FBG written on MOFs using femtosecond laser can be used for high temperature measurement up to 800°C [56]. There are two reflective peaks instead of one peak in the reflection spectrum of an FBG inscribed in birefringent fibers [40, 58, 59]. The separation of these two peaks is directly related to the fiber birefringence.

It is easy to introduce photosensitivity in MOFs by using a germanium-doped rod during the stacking stage. Gratings can be inscribed in MOFs using UV light, and the ease of grating inscription depends on the air-hole patterns. **Figure 6** shows the reflection spectrum of an FBG inscribed in a six-hole suspended-core fiber (SCF) and HB PCF fabricated in our lab. The SEMs of their cross-section are shown in the insets. By optimizing the inscription system, very strong FBGs can be achieved. Owing to the ultrahigh-phase birefringence ($\sim 1.1 \times 10^{-2}$), the two reflective peaks of FBG inscribed in HB PCF show very large wavelength separation of more than 10 nm which is much larger than that in the commercial PM-PCF (0.5 nm) [59] and the HB MOFs (2.1 nm) reported in Ref. [58]. Two peaks with large separation allow for simultaneous measurement of temperature and pressure because the stress transferred to the core along the two polarization axes is different when subjected to pressure.

The FBG inscribed in the six-hole suspended-core fiber can be employed to measure strain and temperature. The measured strain sensitivity is about 0.96 pm/ μm , which is close to that of SMF. Since the germanium is doped in the core as in SMF, similar temperature sensitivity of

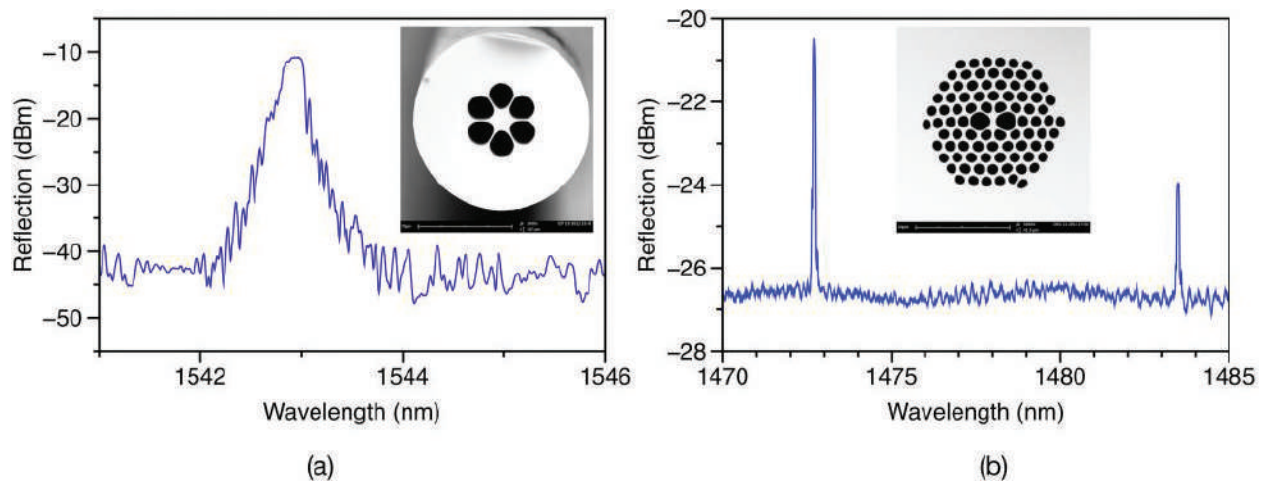


Figure 6. Reflection spectrum of an FBG inscribed in the (a) photosensitive six-hole SCF and (b) HB PCF, adapted from ref. [40], OSA. The insets show the SEM photos of the cross section of the fabricated fibers.

10.7°C was measured. However, the pressure sensitivity of the FBG inscribed in the fiber was measured to be 8.2 pm/MPa, which is higher than that of SMFs, which is ~3.1 pm/MPa [60]. This improvement is due to the six air holes, and further increase in the sensitivity is possible by using larger air holes, as demonstrated in [61]. We designed and fabricated a single-ring suspended fiber, as shown in **Figure 2(h)**, to increase the pressure sensitivity. The measured pressure sensitivity using FBG on this fiber is about 18 pm/MPa, more than 5 times higher than that of standard SMFs.

In addition, the large air holes of MOFs permit materials to be filled in the cladding to functionalize MOFs into a large variety of sensors. For example, low-temperature melting point metal was filled into the air holes of the six-hole SCF to function as anemometer to measure wind speed [22]. The metal absorbs energy from light propagating in the six-hole SCF, and the FBG inscribed in the core measures the temperature change. The cooling rate of the metal/FBG is directly related to the wind speed. Due to the large optical absorption of metal, the heating efficiency is very high, i.e., ~7.3°C/mW. Laser power as low as 14 mW is sufficient to heat the metal/FBG up to 100°C. This is more efficient than the heating process using Co²⁺-doped fiber as we have demonstrated in [62].

3. Sensing applications of MOFs in the oil and gas industry

The demand for fiber optic sensors in the oil/gas industry comes from the harsh downhole conditions and the depth of oil wells which can be as deep as 12 km. The great distance coupled with the high pressure (up to 100 MPa) and temperature (more than 200°C) of oil in downholes restricts the use of conventional sensors. However, the intrinsic features of optical fiber sensors such as long distance transmission, immune to EMI, and high operating temperature make it a promising candidate for the oil industry. The use of multiple FBGs distributed along a single strand of SMF has been employed in oil monitoring. Key parameters like pressure, temperature, and flow speed are widely measured in oil wells [63, 64]. In such

circumstances, high pressure can cause large irretrievable disasters during oil exploitation and oil transportation. Therefore, it is of great importance to measure pressure, and MOFs are potential candidates to enhance the capabilities of optical fiber sensors used in the oil industry.

The stress distribution around the core of MOFs can be tailored via the air-hole pattern to enhance the MOFs' sensitivity to pressure. The application of pressure to MOFs leads to large compression stress in the fiber core where optical light propagates. Good performance in terms of sensitivity, resolution, as well as fast response can be achieved by properly designing the structure of the MOFs.

The basic principle that permits fiber sensors to measure pressure is the photoelastic effect of silica glass. When subjected to pressure, fiber sensors regardless of the use of different operating principles, the silica fiber shows the corresponding dependence on the change in pressure. Particularly, the refractive index of the core/cladding of MOFs varies with applied pressure, which can be expressed as

$$\begin{bmatrix} n_x \\ n_y \\ n_z \end{bmatrix} = n_0 - \begin{bmatrix} C_1 & C_2 & C_2 \\ C_2 & C_1 & C_2 \\ C_2 & C_2 & C_1 \end{bmatrix} \begin{bmatrix} \sigma_x \\ \sigma_y \\ \sigma_z \end{bmatrix}, \quad (8)$$

where n_i is the index component in i_{th} direction ($i = x, y, z$), σ_i represents the corresponding stress component, and n_0 is the silica index without pressure applied. The constants C_1 and C_2 are the stress-optic coefficient for silica glass and have values of 6.5×10^{-13} and $4.2 \times 10^{-12} \text{ m}^2/\text{N}$, respectively. The change in refractive index induced by pressure is determined by the above equation. The pressure-induced change in index is taken into account to calculate the guided mode in MOFs. Either FBGs or interferometry is employed to make pressure sensors, and the stress transfer mechanism is similar. However, in terms of the polarimetric approach based on high birefringence MOFs as introduced in Section 2.3, the resultant pressure sensors that employ the index difference of two polarized modes exhibit better sensitivity.

Figure 7 plots the results of oil pressure measurement using FBGs written on conventional SMF and single-ring suspended fiber (shown in **Figure 2(h)**) with various outer diameters. The single-ring suspended fiber differs from SMF because of the large air region in the fiber, resulting in high air-filling ratio (AFR). AFR of SMF can be regarded as 0, as no air holes exist in the fiber. Typically, higher AFR gives better sensitivity [61]. The measured results using FBG on single-ring suspended fiber show a large improvement (five times) of pressure sensitivity compared to that obtained on SMF. Furthermore, by etching the cladding of the fiber, smaller outer diameter of this MOF means higher AFR and consequently further increases the pressure sensitivity from -18 to -21 pm/MPa .

In addition to improvement in sensitivity, MOFs enable simultaneous measurement of pressure and temperature by using FBG inscribed in high birefringence fiber. As shown in **Figure 6(b)**, the two distinct peaks occurred in the reflection spectrum have a wide wavelength separation due to the large fiber birefringence. The separation is more than 10 nm for this MOF, which has a measured birefringence of 1.1×10^{-2} . Two-parameter measurement tends to be easier when

utilizing two peaks with large separation. **Figure 8(a)** shows the pressure responses of the two modes polarized in fast and slow axes, corresponding to the two FBG peaks located at shorter and longer wavelength, which gives sensitivities of -1.9 pm/MPa for the fast axis peak and -5.1 pm/MPa for the slow axis peak [40]. The different pressure responses obtained from the fast and slow axis peaks are due to the asymmetrical air hole structure, which breaks the uniformity of the pressure-induced stress. Therefore, the stress change along the fast axis is

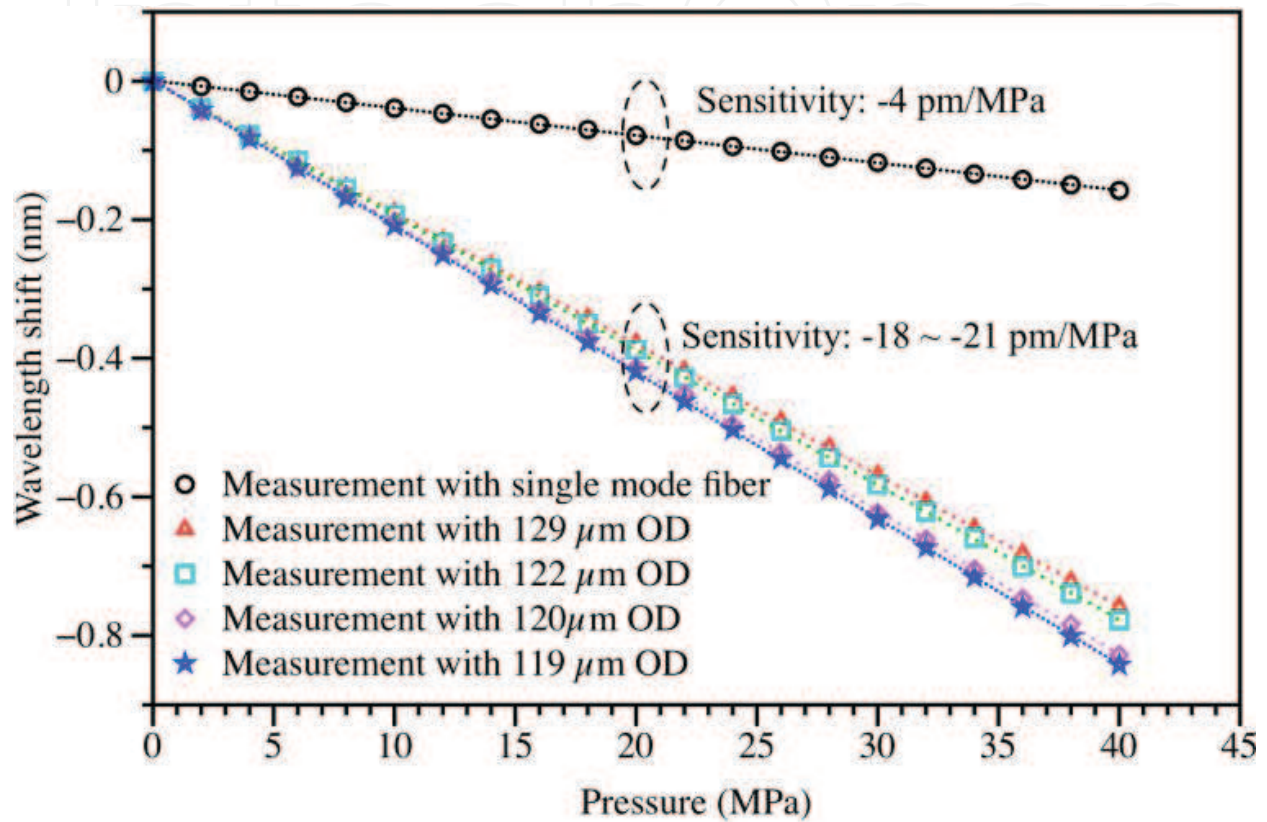


Figure 7. Pressure response of FBGs inscribed in SMF and MOFs.

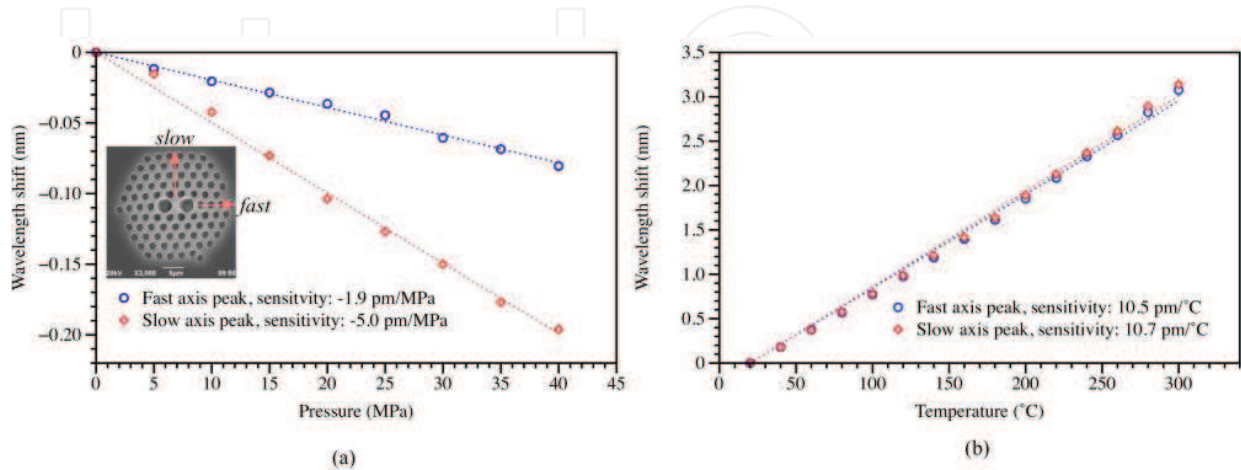


Figure 8. (a) Pressure response of FBG written in the HB-PCF fabricated in our laboratory, where the fast and slow axis peaks show different responses, (b) temperature dependence of the two axes (adapted from Ref. [40], OSA).

smaller than that in the slow axis due to the existence of two large air holes. However, the temperature dependence of the two polarized modes are the same, about $10 \text{ pm}/^\circ\text{C}$, as shown in **Figure 8(b)**. Such discrimination in pressure and temperature allows the simultaneous measurement of these two parameters. The change in pressure and temperature can be calculated according to the total wavelength shift of the fast and slow axis grating peak via the following equation

$$\begin{bmatrix} \Delta T \\ \Delta P \end{bmatrix} = \frac{1}{32.17} \begin{bmatrix} -1.9 & 5.0 \\ -10.5 & 10.7 \end{bmatrix} \begin{bmatrix} \Delta\lambda_s \\ \Delta\lambda_f \end{bmatrix} \quad (9)$$

where $\Delta\lambda_s$ and $\Delta\lambda_f$ are the total wavelength shift for the slow and fast axis grating peaks due to changes in the applied pressure and temperature, respectively.

The pressure sensitivity of FBG sensors is very small, varying from a few to tens of pm/MPa even if special MOFs are employed. The low sensitivity is due to the slight modal index change with respect to pressure. On the other hand, the sensitivity can be improved significantly by applying the polarimetric approaches based on high birefringence MOFs. For example, SI or rocking filter pressure sensors exhibit much higher sensitivity in pressure measurement [65, 66]. The construction of a SI sensor is shown in **Figure 5(a)**, where the MOF is subjected to oil pressure. The oil pressure sensitivity demonstrated by a PM-PCF

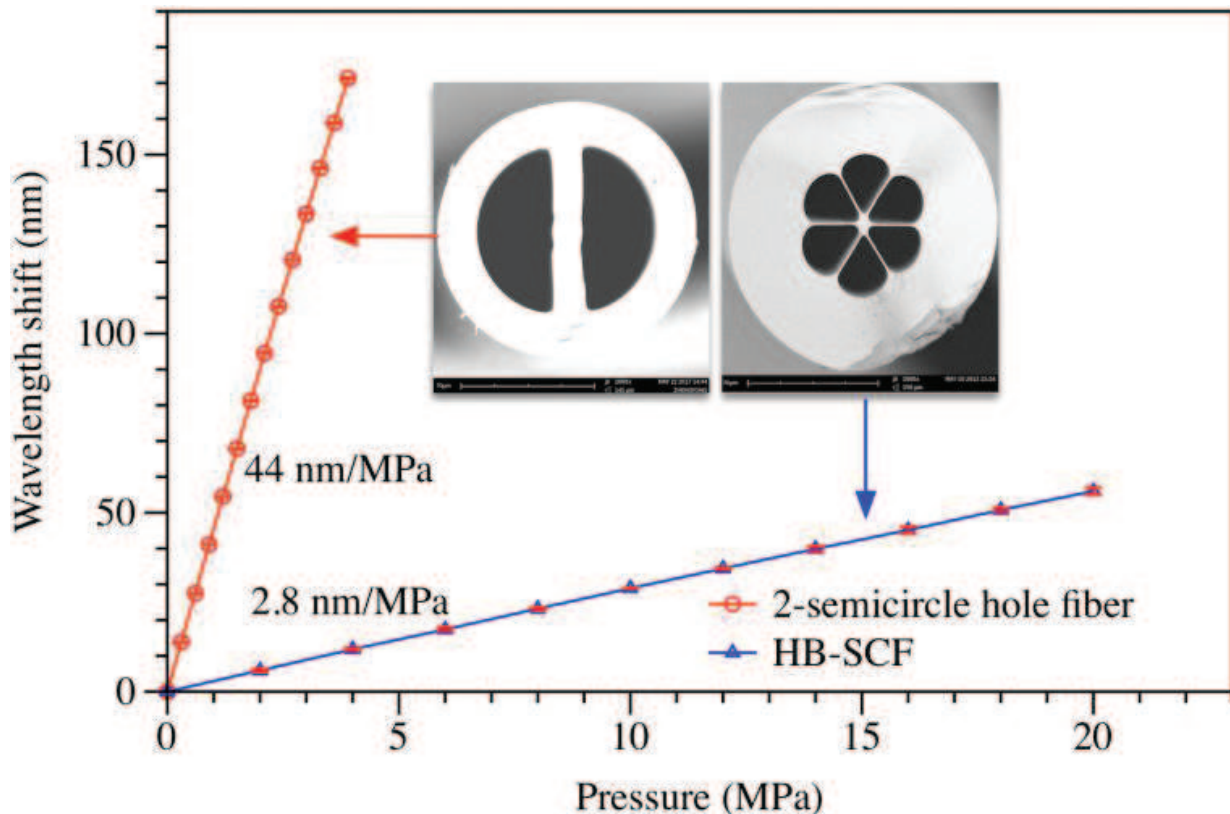


Figure 9. Hydrostatic oil pressure response of Sagnac interferometer realized using HB-SCF [13], (2014 IEEE) and two semicircle hole fiber.

commercially available from NKT Photonics, Inc. is 3.24 nm/MPa at ~1550 nm [67]. The pressure sensitivity of a SI pressure sensor can be written as

$$\frac{d\lambda}{dP} = \frac{\lambda}{G} \frac{dB}{dP'} \quad (10)$$

where the derivative dB/dP represents the phase birefringence change with respect to applied pressure, which means the index difference of two polarized modes is considered rather than only one mode as in the case of FBG sensor. This value can be improved easily by using noncircularly symmetric structure. **Figure 9** shows the wavelength shift as a function of the applied pressure on the highly birefringent MOFs, where (a) plots the results for HB-SCF and (b) is the pressure response for the two semicircle hole fiber. Both measurements are based on SI configuration. The measured pressure sensitivity is ~2.8 nm/MPa using HB-SCF, which is comparable to the commercial PM-PCF. However, the fabrication of HB-SCF is much easier than PM-PCF that has a lot of air holes in honeycomb arrangement [13]. On the other hand, the sensitivity improvement is significant by using the design of two semicircle hole structure, which was measured to be 44 nm/MPa, about 13 times larger than that achieved with commercial PM-PCF. Such great increase owes to the relatively low birefringence (i.e., small G), as well as the cutoff of fast axis by two large semicircle holes (i.e., large dB/dP).

4. Conclusion

To conclude the chapter, several novel structures of optical fibers are proposed and demonstrated for sensing applications. The sensing performance is comparable to and better than most sensors developed based on traditional single-mode fibers (SMFs). The basic fabrication method is briefly reviewed, especially to introduce the asymmetrical stress distribution to MOFs. Due to the novel structure of MOFs, it also exhibits unique feature that SMF does not possess, for instance, the high birefringence. Different air hole structures of MOFs exhibit various mechanical and optical properties that are employed to develop the sensors. The ultrahigh birefringence of HB-PCF can be $\sim 1.2 \times 10^{-2}$, which is the highest one for the fabricated index-guiding PCFs. The pressure sensor based on the fabricated two semicircle hole MOF shows very high sensitivity >40 nm/MPa by constructing a Sagnac interferometer. Those sensors can find good applications in oil and gas industry, as well as the biomedical detection. The demonstrated MOFs can give full understanding of developing sensors to measure physical and biomedical parameters, in terms of the design, fabrication of the MOFs, and the approaches to configure sensors.

Acknowledgements

The authors like to acknowledge the financial support by the Hong Kong Polytechnic University under the project of 1-ZVGB.

Author details

Zhengyong Liu* and Hwa-Yaw Tam

*Address all correspondence to: zhengyong.liu@connect.polyu.hk

Photonics Research Centre, Department of Electrical Engineering, The Hong Kong Polytechnic University, Hung Hum, KLN, Hong Kong

References

- [1] Knight JC. Photonic crystal fibres. *Nature*. 2003;**424**:847-851
- [2] Russell P. Photonic crystal fibers. *Science*. 2003;**299**:358-362
- [3] Russell PSJ. Photonic-crystal Fibers. *Journal of Lightwave Technology*. 2006;**24**:4729-4749
- [4] Knight J, Birks T, Russell P. All-silica single-mode optical fiber with photonic crystal cladding. *Optics Letters*. 1996;**21**:1547-1549
- [5] Birks TA, Knight JC, Russell PS. Endlessly single-mode photonic crystal fiber. *Optics Letters*. 1997;**22**:961-963
- [6] Dudley JM, Coen S. Supercontinuum generation in photonic crystal fiber. *Reviews of Modern Physics*. 2006;**78**:1135-1184
- [7] Toupin P, Brilland L, Renversez G, Troles J. All-solid all-chalcogenide microstructured optical fiber. *Optics Express*. 2013;**21**:14643
- [8] <http://www.nktphotonics.com/lasers-fibers/en/>
- [9] Kong F, et al. Polarizing ytterbium-doped all-solid photonic bandgap fiber with $\sim 1150\mu\text{m}^2$ effective mode area. *Optics Express*. 2015;**23**:4307
- [10] Groothoff N, Canning J, Ryan T, Lyytikainen K, Inglis H. Distributed feedback photonic crystal fibre (DFB-PCF) laser. *Optics Express*. 2005;**13**:2924-2930
- [11] Canning J, et al. All-fibre photonic crystal distributed Bragg reflector (PC-DBR) fibre laser. *Optics Express*. 2003;**11**:1995-2000
- [12] Liu Z, et al. Intermodal coupling of supermodes in a twin-core photonic crystal fiber and its application as a pressure sensor. *Optics Express*. 2012;**20**:21749-21757
- [13] Liu Z, Wu C, Tse M-LV, Tam H-Y. Fabrication, characterization, and sensing applications of a high-birefringence suspended-core fiber. *Journal of Lightwave Technology*. 2014;**32**: 2113-2122
- [14] Monro TM, et al. Sensing with microstructured optical fibres. *Measurement Science and Technology*. 2001;**12**:854-858

- [15] Liu Z, Tam H-Y, Htein L, Tse M-LV, Lu C. Microstructured optical Fiber sensors. *Journal of Lightwave Technology*. 2017;**35**:3425-3439
- [16] Pinto AMR, Lopez-Amo M. Photonic crystal Fibers for sensing applications. *Journal of Sensors*. 2012;**2012**:1-21
- [17] Fu HY, et al. Pressure sensor realized with polarization-maintaining photonic crystal fiber-based Sagnac interferometer. *Applied Optics*. 2008;**47**:2835-2839
- [18] Jin W, Cao Y, Yang F, Ho HL. Ultra-sensitive all-fibre photothermal spectroscopy with large dynamic range. *Nature Communications*. 2015;**6**:6767
- [19] Bykov DS, Schmidt OA, Euser TG, Russell PSJ. Flying particle sensors in hollow-core photonic crystal fibre. *Nature Photonics*. 2015;**9**:1-14
- [20] Cubillas AM, et al. Photonic crystal fibres for chemical sensing and photochemistry. *Chemical Society Reviews*. 2013;**42**:8629-8648
- [21] Wu C, et al. In-line microfluidic refractometer based on C-shaped fiber assisted photonic crystal fiber Sagnac interferometer. *Optics Letters*. 2013;**38**:3283-3286
- [22] Wang J, et al. Fiber-optic anemometer based on Bragg grating inscribed in metal-filled microstructured optical Fiber. *IEEE Xplore: Journal of Lightwave Technology*. 2016;**34**:4884-4889
- [23] Sun B, et al. Microstructured-core photonic-crystal fiber for ultra-sensitive refractive index sensing. *Optics Express*. 2011;**19**:4091-4100
- [24] Ebendorff-Heidepriem H, Warren-Smith S. Suspended nanowires: Fabrication, design and characterization of fibers with nanoscale cores. *Optics Express*. 2009;**17**:2646-2657
- [25] Large MCJ, et al. Microstructured polymer optical fibres: New opportunities and challenges. *Molecular Crystals and Liquid Crystals*. 2006;**446**:219-231
- [26] El-Amraoui M, et al. Microstructured chalcogenide optical fibers from As₂S₃ glass: Towards new IR broadband sources. *Optics Express*. 2010;**18**:26655-26665
- [27] Tse M-LV, et al. Superlattice microstructured optical Fiber. *Materials (Basel)*. 2014;**7**:4567-4573
- [28] Chen D, Vincent Tse ML, Tam HY. Super-lattice structure photonic crystal fiber. *Progress in Electromagnetics Research*. 2010;**11**:53-64
- [29] Fitt A, Furusawa K, Monro T. The mathematical modelling of capillary drawing for holey fibre manufacture. *Journal of Engineering Mathematics*. 2002;**43**:201-227
- [30] Htein L, Liu Z, Tam HY. Hydrostatic pressure sensor based on fiber Bragg grating written in single-ring suspended fiber. *Proc. SPIE 9916, Sixth Eur. Work. Opt. Fibre Sensors 99161R*; 2016. DOI:10.1117/12.2235842
- [31] Chen D, Hu G, Chen L. Dual-core photonic crystal Fiber for hydrostatic pressure sensing. *IEEE Photonics Technology Letters*. 2011;**23**:1851-1853

- [32] Zhang L. Polarization-dependent coupling in twin-core photonic crystal fibers. *Journal of Lightwave Technology*. 2004;**22**:1367-1373
- [33] Tse MLV, et al. Fusion splicing holey Fibers and single-mode Fibers: A simple method to reduce loss and increase strength. *IEEE Photonics Technology Letters*. 2009;**21**:164-166
- [34] Xiao L, Jin W, Demokan MS. Fusion splicing small-core photonic crystal fibers and single-mode fibers by repeated arc discharges. *Optics Letters*. 2007;**32**:115-117
- [35] Noda J, Okamoto K, Sasaki Y. Polarization-maintaining fibers and their applications. *Journal of Lightwave Technology*. 1986;**4**:1071-1089
- [36] Zhu M, Murayama H, Wada D, Kageyama K. Dependence of measurement accuracy on the birefringence of PANDA fiber Bragg gratings in distributed simultaneous strain and temperature sensing. *Optics Express*. 2017;**25**:4000
- [37] Dong X, Tam HY, Shum P. Temperature-insensitive strain sensor with polarization-maintaining photonic crystal fiber based Sagnac interferometer. *Applied Physics Letters*. 2007;**90**:151113
- [38] Chen T, et al. Distributed high-temperature pressure sensing using air-hole microstructural fibers. *Optics Letters*. 2012;**37**(6):1064
- [39] Weiguo C, et al. Highly sensitive torsion sensor based on Sagnac interferometer using side-leakage photonic crystal Fiber. *IEEE Photonics Technology Letters*. 2011;**23**:1639-1641
- [40] Liu Z, Wu C, Tse M-LV, Lu C, Tam H-Y. Ultrahigh birefringence index-guiding photonic crystal fiber and its application for pressure and temperature discrimination. *Optics Letters*. 2013;**38**:1385-1387
- [41] Suzuki K, Kubota H, Kawanishi S, Tanaka M, Fujita M. Optical properties of a low-loss polarization-maintaining photonic crystal fiber. *Optics Express*. 2001;**9**:676-680
- [42] Edahiro T, Sasaki Y, Hosaka T, Miya T, Okamoto K. Low-loss single polarisation fibres with asymmetrical strain birefringence. *Electronics Letters*. 1981;**17**:530-531
- [43] Birch RD, Payne DN, Varnham MP. Fabrication of polarisation- maintaining fibres using gas-phase etching. *Electronics Letters*. 1982;**18**:1036-1038
- [44] Ortigosa-Blanch A, Knight J, Wadsworth W. Highly birefringent photonic crystal fibers. *Optics Letters*. 2000;**25**:1325-1327
- [45] Frazão O, et al. Simultaneous measurement of multiparameters using a Sagnac interferometer with polarization maintaining side-hole fiber. *Applied Optics*. 2008;**47**:4841-4848
- [46] Kim S, et al. Ultrahigh birefringence of elliptic core fibers with irregular air holes. *Journal of Applied Physics*. 2007;**102**:16101
- [47] Martynkien T, et al. Highly birefringent microstructured fibers with enhanced sensitivity to hydrostatic pressure. *Optics Express*. 2010;**18**:15113-15121

- [48] Beltrán-Mejía F, et al. Ultrahigh-birefringent squeezed lattice photonic crystal fiber with rotated elliptical air holes. *Optics Letters*. 2010;**35**:544-546
- [49] Hansen TP, et al. Highly birefringent index-guiding photonic crystal fibers. *IEEE Photonics Technology Letters*. 2001;**13**:588-590
- [50] Shi J, Feng X, Horak P, Poletti F. A fiberized highly birefringent glass micrometer-size ridge waveguide. *Optical Fiber Technology*. 2015;**23**:137-144
- [51] Ortigosa-Blanch A. Ultrahigh birefringent nonlinear microstructured fiber. *IEEE Photonics Technology Letters*. 2004;**16**:1667-1669
- [52] Chen X, et al. Highly birefringent hollow-core photonic bandgap fiber. *Optics Express*. 2004;**12**:3888-3893
- [53] Pei T-H, Zhang Z, Zhang Y. The high-birefringence asymmetric SF57 glass microstructured optical fiber at 1060.0 μm . *Optical Fiber Technology*. 2017;**36**:265-270
- [54] Caillaud C, et al. Highly birefringent chalcogenide optical fiber for polarization-maintaining in the 3-8.5 μm mid-IR window. *Optics Express*. 2016;**24**:7977
- [55] Hill KO, Meltz G. Fiber Bragg grating technology fundamentals and overview. *Journal of Lightwave Technology*. 1997;**15**:1263-1276
- [56] Jewart CM, et al. Ultrafast femtosecond-laser-induced fiber Bragg gratings in air-hole microstructured fibers for high-temperature pressure sensing. *Optics Letters*. 2010;**35**:1443-1445
- [57] Groothoff N, Canning J, Buckley E, Lyttikainen K, Zagari J. Bragg gratings in air-silica structured fibers. *Optics Letters*. 2003;**28**:233-235
- [58] Geernaert T, et al. Fiber Bragg gratings in germanium-doped highly birefringent microstructured optical fibers. *IEEE Photonics Technology Letters*. 2008;**20**:554-556
- [59] Guan B, Chen D, Zhang Y. Bragg gratings in pure-silica polarization-maintaining photonic crystal fiber. *IEEE Photonics Technology Letters*. 2008;**20**:1980-1982
- [60] Xu M, Reekie L, Chow Y, Dakin JP. Optical in-fibre grating high pressure sensor. *Electronics Letters*. 1993;**29**:398-399
- [61] Wu C, Guan B-O, Wang Z, Feng X. Characterization of pressure response of Bragg gratings in grapefruit microstructured Fibers. *Journal of Lightwave Technology*. 2010;**28**:1392-1397
- [62] Liu Z, Tse MV, Zhang AP, Tam H. Integrated microfluidic flowmeter based on a micro-FBG inscribed in Co²⁺-doped optical fiber. *Optics Letters*. 2014;**39**:5877-5880
- [63] Kersey AD. Optical fiber sensors for permanent downwell monitoring applications in the oil and gas industry. *IEICE Transactions on Electronics*. 2000;**83**:400-404

- [64] Nakstad H, Kringlebotn JT. Oil and gas applications: Probing oil fields. *Nature Photonics*. 2008;**2**:147-149
- [65] Anuszkiewicz A, et al. Sensing characteristics of the rocking filters in microstructured fibers optimized for hydrostatic pressure measurements. *Optics Express*. 2012;**20**:23320
- [66] Kakarantzas G, et al. Structural rocking filters in highly birefringent photonic crystal fiber. *Optics Letters*. 2003;**28**:158-160
- [67] Fu HY, et al. High pressure sensor based on photonic crystal fiber for downhole application. *Applied Optics*. 2010;**49**:2639-2643

IntechOpen

We are IntechOpen, the world's leading publisher of Open Access books Built by scientists, for scientists

6,300

Open access books available

171,000

International authors and editors

190M

Downloads

Our authors are among the

154

Countries delivered to

TOP 1%

most cited scientists

12.2%

Contributors from top 500 universities



WEB OF SCIENCE™

Selection of our books indexed in the Book Citation Index
in Web of Science™ Core Collection (BKCI)

Interested in publishing with us?
Contact book.department@intechopen.com

Numbers displayed above are based on latest data collected.
For more information visit www.intechopen.com



Photonic Crystal Fiber–Based Interferometric Sensors

Dora Juan Juan Hu, Rebecca Yen-Ni Wong and
Perry Ping Shum

Additional information is available at the end of the chapter

<http://dx.doi.org/10.5772/intechopen.70713>

Abstract

Photonic crystal fibers (PCFs), also known as microstructured optical fibers, are a highlighted invention of optical fiber technology which have unveiled a new domain of manipulating light in engineered fiber waveguides with unparalleled flexibility and controllability. Since the report of the first fabricated PCF in 1996, research in PCFs has resulted in numerous explorations, development and commercialization of PCF-based technologies and applications. PCFs contain axially aligned air channels which provide a large degree of freedom in design to achieve a variety of peculiar properties; numerous PCF-based sensors have been proposed, developed and demonstrated for a broad range of sensing applications. In this chapter, we will review the field of research on design, development and experimental achievement of PCF-based interferometric sensors for physical and biomedical sensing applications.

Keywords: photonic crystal fibers, interferometry, fiber optic sensors, Fabry-Perot interferometer, Mach-Zehnder interferometer, Michelson interferometer, Sagnac interferometer

1. Background

Optical fiber interferometric sensors have been widely used for various sensing applications and characterization of physical magnitudes. The advantages provided by optical fibers have been well recognized and utilized in interferometric sensor applications, which include compactness, alignment freedom from free space optics, high sensitivity, high reliability etc. [1]. Photonic crystal fibers (PCFs), a highlighted fiber technology that was first invented and demonstrated in 1996, have brought breakthroughs in communications, sensing, defense and medicine [2]. These fibers have demonstrated superior features in many applications and created substantial scientific and industrial impact in recent years. In the past decade, PCFs have received intensive and continuous attention, and undergone rapid development from

design and fabrication to device realization and commercialization. Compared to conventional optical fibers, PCFs represent a more versatile platform to construct interferometry sensors because of enhanced flexibility in manipulating optical properties and light-medium interactions. Various PCF structures, such as polarization-maintaining (PM) PCFs, photonic bandgap (PBG) PCFs including hollow core (HC) PCFs and all-solid PBG PCFs, Bragg fibers, large mode area (LMA) PCFs and highly nonlinear PCFs have been demonstrated with good potential in developing interferometric fiber sensors. PCFs can provide a platform for integration of materials such as gas, fluid or metals for additional functionality. For example, PCFs have been exploited for optofluidic sensing and gas sensing applications utilizing the selective or unselective infiltration of fluid or gas in the holey structures [3]. In addition, they are a desirable platform for the incorporation of plasmonic structures that can enhance application opportunities in terms of performance as well as versatility. Integration of plasmonic structures such as metal nanoparticles, metal nanowires, and metal thin films in PCF structures have proven to substantially improve sensor performance, e.g. sensitivity [4]. The continuing development and maturation of PCF technologies and PCF-based interferometric sensors are expected to make more contributions to optical fiber technology and real world applications [5].

2. Overview of PCF-based interferometric sensors

In this chapter, various configurations of interferometry sensors based on PCFs and their sensing applications are demonstrated, namely Fabry-Perot interferometer (FPI), Mach Zehnder interferometer (MZI), Michelson interferometer and Sagnac interferometer. Compared to standard optical fibers, PCF structures possess many interesting characteristics and tunable properties which are highly desirable when constructing interferometric sensors with enhanced performance.

2.1. Fabry-Perot interferometer (FPI)

A Fabry-Perot interferometer is comprised of a cavity (or etalon) made of two highly reflective surfaces/mirrors which enable light propagating down the fiber to be partially reflected. The transmitted, and subsequently, reflected beams will form an interference pattern due to the difference in phase delay.

The reflection coefficients, R_i , at the mirrors can be defined by [6]:

$$R_i = \left(\frac{n_i - n_{i+1}}{n_i + n_{i+1}} \right)^2, i = 1, 2, 3, \dots \quad (1)$$

where n_i is the refractive index of the cavity and surrounding medium.

The phase difference, δ , of the interferometer can be represented by [1]:

$$\delta = \frac{2\pi}{\lambda} n2L \quad (2)$$

where λ is the incident light wavelength and L is the physical length of the cavity.

FPIs can typically be classed as either extrinsic or intrinsic, depending on their make-up. Extrinsic FPIs (EFPI), as shown in **Figure 1(a)**, use the air gap between two fibers and reflects light between the cleaved ends. The cavity of intrinsic FPIs (IFPI) is formed within the fiber itself, where the two reflectors lie along the length of the fiber [1], as shown in **Figure 1(b), (c)**. IFPIs can have advantages over EFPIs such as higher coupling efficiency.

For IFPIs, the etalon/cavity can be formed by fusion splicing a section of HC-PCF, which acts as the cavity, between two lengths of single mode fiber with cleaved end surfaces [7]. This configuration allows for a customizable cavity length, which can be a few micrometers or a few centimeters long [7]. Villatoro presented a spherical FP cavity by means of a microscopic air bubbles (20–58 μm diameters) fabricated via arc discharge between a standard SMF and a PCF. This technique can reduce the number of steps required for fabricating FPIs [8]. Favero et al. [9] pressurized the holes in the PCF to produce reproducible elliptical bubbles with controllable cavity dimensions.

Hu et al. [6] were able to realize a refractive index tip sensor used in reflection mode. This sensor was based on a hollow silica sphere with a thin silica wall being formed at one end of a simplified HCF via means of arc discharge, as shown in **Figure 2**. The reflected spectrum was modulated by the interaction between the sensor head and the environment (refractive index (RI) and temperature). A RI resolution of 6.2×10^{-5} , using fringe visibility (**Figure 2 (c)**), was determined and the temperature sensitivity for the high and low frequency fringes were 1.3 and 17 $\text{pm}/^\circ\text{C}$, respectively (**Figure 2 (d)**), at temperatures up to $\sim 1000^\circ\text{C}$.

Micro FP cavities can offer low cross sensitivity with temperature, yet high RI sensitivity. A RI sensor was realized by drilling micro-holes into a simplified hollow core (SHC) PCF micro

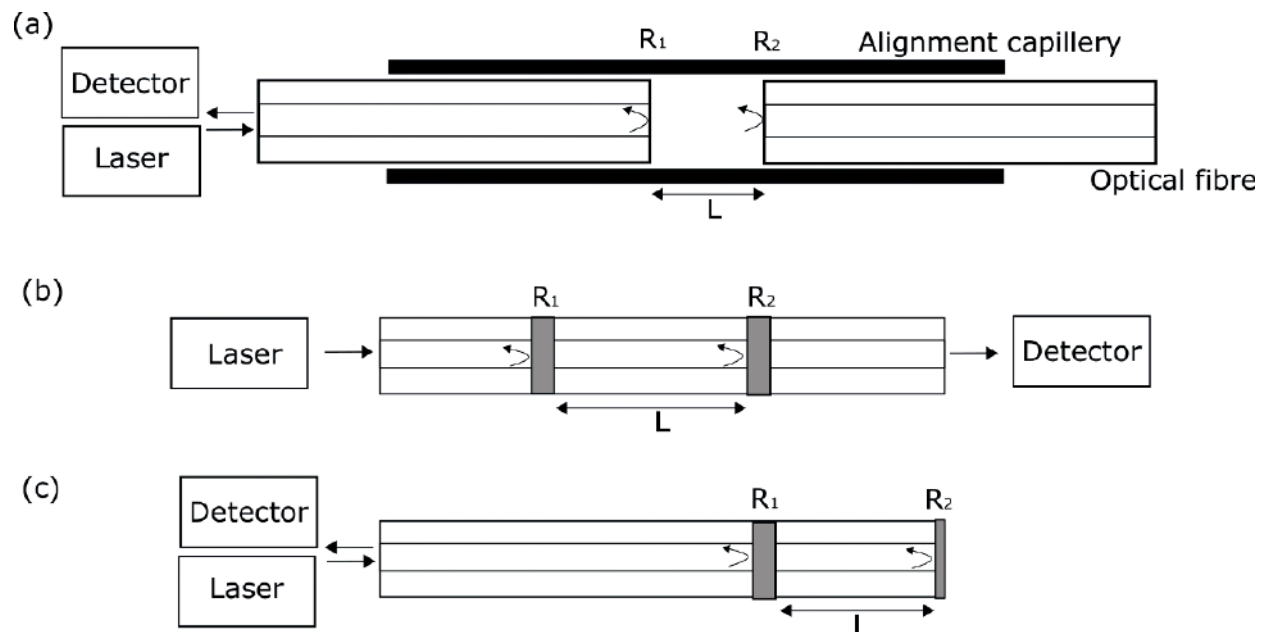


Figure 1. (a) The schematic of an extrinsic Fabry-Perot interferometer; (b) the schematic of an intrinsic Fabry-Perot interferometer; (c) the schematic of an intrinsic Fabry-Perot interferometer working in reflection mode. R_i represents the reflective surfaces and L is the length of the cavity.

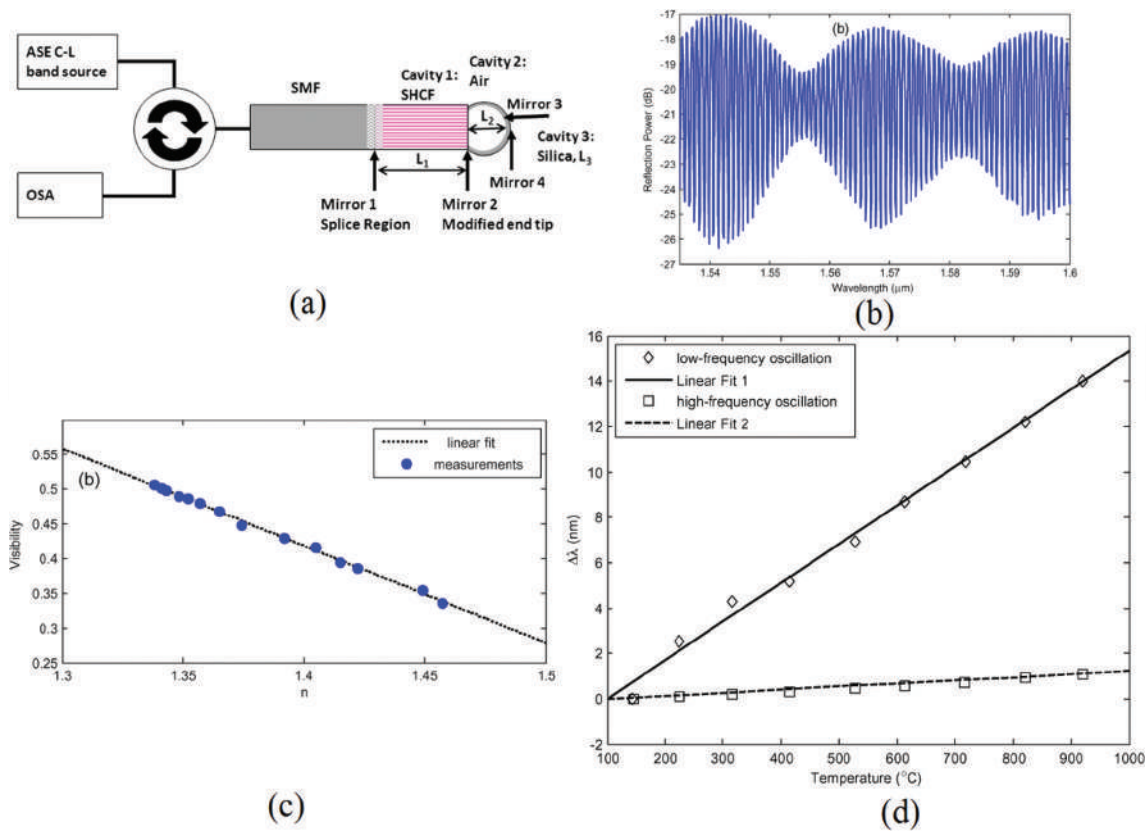


Figure 2. (a) Configuration of the simplified HCF based IFPI working in reflection mode; (b) interference spectrum of the sensor head; (c) refractive index against fringe visibility. (d) Temperature sensitivity against wavelength shift for low and high frequency oscillations. © 2012 IEEE. Reprinted, with permission, from Ref. [6].

cavity using a femtosecond laser to allow the analyte to enter the cavity [10]. A RI sensitivity of ~ 851 nm/RIU and a low cross sensitivity with temperature of $\sim 3.2 \times 10^{-7}$ RIU/ $^{\circ}\text{C}$ was obtained. A short section of hollow fiber had been sandwiched between single mode fiber (SMF) and solid core (SC) PCF [11]. By taking advantage of the air holes in PCF, air was allowed to infiltrate the PCF cavity and the RI changes under different pressures were measured. When creating hole collapse regions between a section of SMF and PCF, the length of the region can affect the sensitivity of the sensor to RI and also temperature. A longer collapsed area will lead to more cladding modes being excited and in turn larger changes in the interference pattern. Dash and Jha [12] found that as they increased the length of the collapsed region from 180 to 270 μm , the RI sensitivity also increased from 30 to 53 nm/RIU with a RI resolution of 1.18×10^{-4} RIU.

A Microbubble FPI has been shown as a strain and vibration sensor with a spheroidal cavity achieving a strain sensitivity of ~ 10.3 pm/ $\mu\epsilon$ and high fringe visibility (~ 38 dB) [13]. A 157 nm laser was used for micromachining an in-line etalon, with two smooth and parallel reflecting sides, in an endlessly single mode PCF. This was demonstrated for strain measurements in a high temperature environment with a fringe contrast of ~ 26 dB [14]. Shi et al. [15] were able to produce a multiplexed strain sensor system using different lengths of HCF spliced between SMF. Due to their wide free spectral range, the signals could be easily demodulated using fast Fourier transform (FFT). A strain insensitive IFPI has been developed by splicing one end of a

solid PCF to a SMF and the other end to a HC-PCF to form a micro cavity. A large portion of the strain sensitivity comes from changing the size of the micro cavity, but in this case, this was at the end of the sensor and remained fixed in size [12].

Due to the all silica structure of PCFs, they are able to withstand high temperatures [6, 16], often for long periods of time [17]. The sensitivity to temperature is often based on the thermal-optic effect of silica and is therefore proportional to the length of the PCF cavity [18]. Frazão et al. [18] characterized the strain and temperature sensitivities of suspended core fibers with three and four holes. The normalized temperature sensitivities were found to be similar at 67.8 and 67.6 rad/m°C for three and four holes, respectively. The strain response was found to be greater for the three hole fiber. This was because the strain was applied to the cladding region (supporting walls of the fiber), and this cross-section was smaller for the three hole fiber.

Wu et al. were able to successfully demonstrate a high pressure (up to 40 MPa) and high temperature FPI (up to 700°C) sensor. A SC-PCF was spliced to one end to a SMF and hole collapse was carried out at the other end, to improve the reflectivity of the second mirror. The pressure and temperature sensitivities were -5.8 and ~ 13 pm/°C, respectively [19]. PCF based IFPIs may also have potential use in photonic integrated circuits [20].

2.2. Mach-Zehnder interferometer (MZI)

The Mach-Zehnder interferometer (MZI) works where an incident beam from a single light source is split into two arms and later recombined, forming an interference pattern [1]. When there is a perturbation in one arm, the difference in optical path length changes and is conveyed by the variation in the interference signal.

A MZI can be fabricated using two fibers with the light being split and recombined using fiber couplers, as shown in **Figure 3(a)**. One beam is referred to as the reference arm, and the other the sensing arm. To fabricate an in-line MZI using a singular fiber, as in **Figure 3(b)**, modal dispersion is used and the propagating modes are coupled into the cladding as well as the core. Though the physical length of the two arms is the same the phase velocity is different as the effective indices of the core and cladding are not the same.

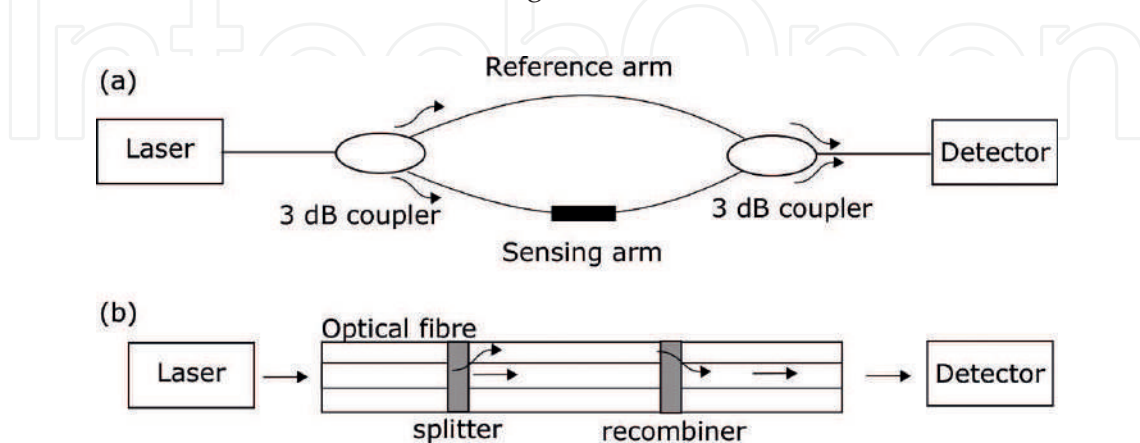


Figure 3. (a) The schematic of a Mach-Zehnder interferometer using two fibers; (b) the schematic of an in-line Mach-Zehnder interferometer using one fiber.

The Mach-Zehnder sensor interference spectrum can be expressed as [21]:

$$I = I_1 + I_2 + 2\sqrt{I_1 I_2} \cos \Delta\phi \quad (3)$$

where I_1 and I_2 are the irradiance of the interfering waves, $\Delta\phi$ is the phase difference between the core and cladding mode is defined as:

$$\Delta\phi = \frac{2\pi}{\lambda} \Delta n L + \Phi \quad (4)$$

where λ is the wavelength, L is the optical length of the interferometer, Δn is the difference in effective refractive index and Φ is the initial phase difference of the two waves.

PCF MZIs commonly consist of a SMF-PCF-SMF configuration; where a small section of solid core PCF is spliced between two standard SMFs. By using a fusion splicer to collapse the air holes of the PCF, the light is no longer constrained to the core and some of the light is coupled to one or multiple cladding modes and are able to propagate along the fiber [22, 23]. The splice points act as the mode couplers to form the fiber MZI, where the first splice point causes light from the core to couple to the cladding and the second splice causes the modes to recombine. MZIs composed entirely of LMA-PCF have also been realized [22] by core misalignment or by hole collapsing, as shown in **Figure 4**. By using the hole collapse technique in an all PCF MZI, alignment is less stringent as no cleaving is required. More cladding modes will also be excited and when the interference spectra were Fourier transformed, multiple spatial frequencies were seen with the number increasing with increasing interferometer length [22]. Different lengths of PCF were studied and compared for sensitivity [23–25]. It was found that the sensitivity was

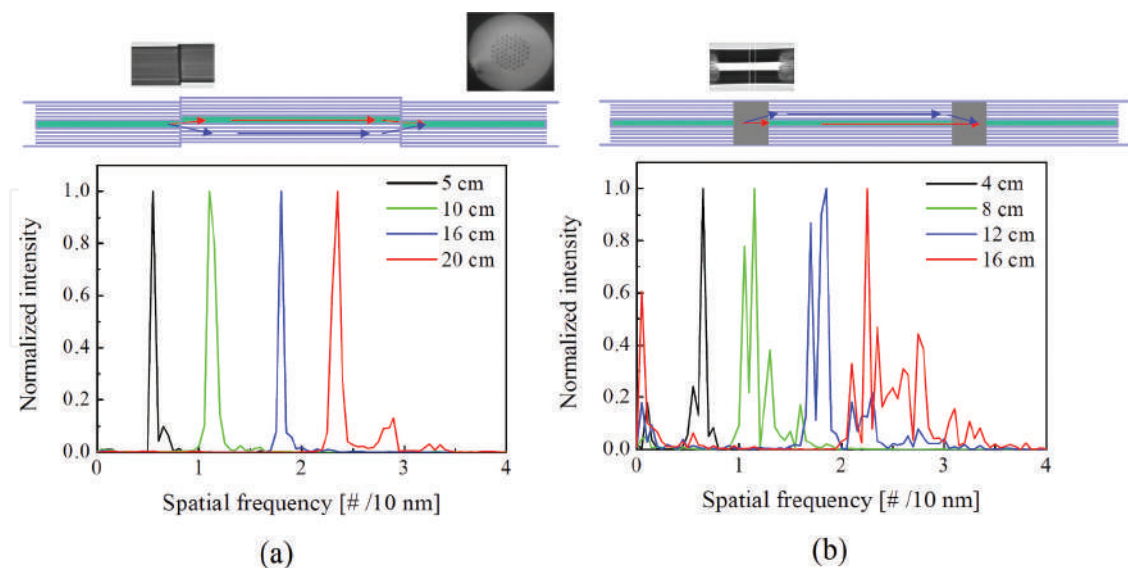


Figure 4. (a) The offset splicing method and the corresponding spatial frequencies at different interferometer lengths. Inset: Cross section of the LMA-PCF; (b) the hole collapse method and the corresponding spatial frequencies at different interferometer lengths. (a) produced one dominant spatial frequency at each length, whereas (b) induced several. Reprinted with permission from Ref. [22]. Copyright 2007 Optical Society of America.

not strongly dependent on length, though longer sections could require better handling and packaging.

These MZI configurations make useful refractometers as the effective refractive index of the cladding modes will be influenced by the surrounding environment [21, 23]. Highly sensitive refractometers have been demonstrated by means of tapering, either at just the splice points [26, 27] or the entire PCF section [28] to expose the evanescent field, making the MZI more sensitive to external RI changes. By tapering at the splice point, when compared to direct splicing, Wang et al. [27] was able to increase the sensor sensitivity from 224.2 to 260.8 nm/RIU. Wong et al. [29] used a combination of PCF-MZI and cavity ring-down technique for signal demodulation, which lead to a minimum detectable RI to be 7.8×10^{-5} RIU, almost 2.5 times greater than when compared to a PCF-MZI based on wavelength demodulation.

PCFs are generally known to be relatively temperature insensitive due to their small thermo-optic coefficient. Methods used to increase this sensitivity include, partial [30] or full [31] liquid infiltration into the holey region of the PCF, and multipath (more than two) MZIs using multicore PCFs [32] as this improves the phase sensitivity. Zhao et al. were able to achieve a temperature sensitivity of 130.6 pm/°C [32].

Different PCF configurations have been used for measuring strain [25, 33–35]. By using a multimode PCF, and careful hole collapse during splicing, a MZI was realized by coupling to two different core modes, LP_{01} and LP_{31} , allowing the light to be confined within the core and not as susceptible to ambient environment. Zheng et al. [25] were able to demonstrate a temperature and RI insensitive strain sensor with a sensitivity of 2.1 pm/ $\mu\epsilon$ at 1550 nm with a 45 mm long PCF between two lengths of SMF. By introducing an additional collapsed region in the center of the length of PCF, two cascaded MZIs were created; the extinction ratio of the MZI induced fringes and in turn the measurement accuracy was improved [34]. The sensitivities for a normal SMF-PCF-SMF MZI and the modified MZI were 1.87 and 11.22 dB/m ϵ , respectively. With twin core (TC) PCFs, the two cores can each act as the arm of the interferometer [36] and allow for a large strain measurement range as there are no deformations in the PCF to weaken the structure [33].

TC-PCFs have also been successfully demonstrated for use as intensity-based bend sensors [36], with a signal change found when the fiber is bent, such that both cores will experience different bend radii. Sun et al. [37] proposed a sensitive bend sensor by introducing an up- or peanut like -taper as the splitter and a down-taper as the recombiner. The up-taper improves the coupling between the PCF core and cladding modes and produces a stronger interference signal when recombined. The bend sensitivity of 50.5 nm/m¹ is one order of magnitude greater, when compared to a PCF MZI with a configuration of hole collapse and core offset (3.046 nm/m¹) [38].

The addition of a functional coating can lead to more specific and tailored sensing applications. As shown by Tao et al. [39], by coating the holey region of large mode area (LMA) and a grapefruit PCF with a polyallylamine layer with an affinity towards TNT vapor, they were able to selectively detect TNT. The LMA PCF had a lower a detection limit of 0.2 ppb_v due to a higher Q-factor. Lopez-Torres et al. demonstrated a humidity sensor capable of resolving

0.074% of relative humidity, and used a method based on the fast Fourier transform to yield a more linear device response with less noise [40]. Functionalized tip sensors have been used to detect changes in pH level [41] and changes in RI [42]. By modifying the surface of a compact PCF (~3 mm long) sensing region with biotin, Hu et al. were able to successfully demonstrate streptavidin detection [43]. Surface modified sensors can be more advantageous over air hole modification as it can be easily cleaned, reused and the analyte response is faster [43].

Long period gratings (LPGs) have also been used to fabricate in-line MZIs as they work by coupling forward propagating core light with one or more co-propagating cladding modes. This has been extended for use in all-PCF MZIs [44, 45]. Mechanically induced LPGs allow for identical, yet tuneable non-permanent LPGs to be fabricated. Yu et al. [45] demonstrated that the first LPG could be replaced by a misaligned splice point. As this is easier to manufacture than an LPG, it could reduce fabrication time and cost. The interference pattern can be tuned by adjusting the offset or the distance between the splitter and combiner [45] as well as the period and strength of the gratings [44]. It is also possible to replace the second LPG by collapsing the holes of the PCF [46]. Compact LPG based MZIs have been demonstrated, by using a CO₂ laser [35, 47] to create periodic grooves until both LPGs have coupling efficiency of around 3 dB. Compared with a standard single mode fiber MZI, Ju et al. [47] were able to obtain a higher strain sensitivity ($-2.6 \text{ pm}/\mu\epsilon$ compared to $+0.445 \text{ pm}/\mu\epsilon$) and a lower temperature sensitivity ($42.4 \text{ pm}/^\circ\text{C}$ per m compared to $1215.56 \text{ pm}/^\circ\text{C}$ per m). MZIs made with LPGs can be at risk of having a high insertion loss [24] due the deformation of fiber structure from inscription or from the misaligned splice point [45]. By cascading an LPG with a PCF MZI, simultaneous temperature and RI sensing was achieved as both elements in the sensor matrix responded differently to the multiple parameters [48].

Measuring low acoustic frequencies underwater can be difficult due to poor signal-to-noise ratios. An optical fiber based hydrophone using a polarization maintaining (PM) PCF sandwiched between SMFs was able to detect frequencies ranging from 5 to 200 Hz. The MZI used a two parameter detection method, namely a change in the intensity of the signal and a shift in wavelength. The change in power ranged from 0.8 to 2.32 dBm, which was much higher when compared to the ~0.1 dBm change using a SMF-MMF-SMF configuration [49].

PCF-MZIs also have potentials in communications for the demodulation of signals using differential phase shift keying (DPSK) [50] and in wavelength-division multiplexing (WDM) [51].

2.3. Michelson interferometer

Optical fiber Michelson interferometers can be realized by using two fibers or one fiber with the configurations shown in **Figure 5**. They are a similar version of MZI configurations. In the two fibers configuration, the laser light is split into two optical paths by an optical fiber coupler. The light is reflected back by the mirrors and recombined at the coupler to form the interference at the detector. In the one fiber configuration, the modes are split at a region where higher order modes or cladding modes are excited, e.g. splicing region between SMF and PCF, and are reflected by the mirrors and recombined at the splicing regions to form the interference which passes to the detector via a circulator.

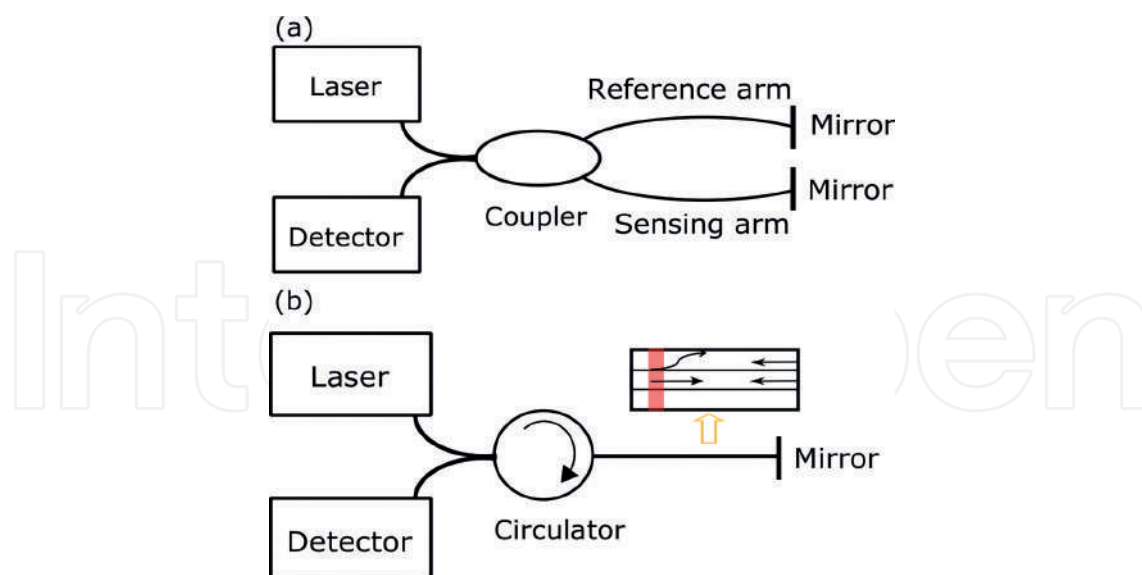


Figure 5. (a) The schematic of a Michelson interferometer using two fibers; (b) the schematic of a Michelson interferometer using one fiber.

Most PCF-based Michelson interferometers are based on one-fiber configurations. PM-PCFs have two orthogonally polarized core modes which act as two different optical paths for interference [52]. The two different optical paths can also be formed by two core modes in two-core PCFs [53, 54], or two core fibers [55]. In addition, the core mode and cladding modes that are excited at the splicing region between a SMF and a PCF due to mode mismatch [56] or a collapsed region in PCFs [57–62]. Similar configurations have also been reported in thin core fibers [63]. Due to the flexibility in the waveguide properties, PCF-based configurations can achieve high sensitivities when measuring ambient parameters, such as RI, temperature etc.

Jha et al. presented a Michelson interferometer device using a stub of a LMA PCF, with the schematic of the experimental setup and the interference spectrum in the reflected signal as shown in **Figure 6**. The PCF was fully collapsed at the splicing region between SMF and PCF, forming a multimode region for cladding mode excitation, and the end of the PCF was behaving as a reflective mirror. The dependence of the PCF length, temperature and ambient RI on the interference fringes of the device was investigated for sensing applications [58].

Enhanced temperature sensitivity was reported using a liquid-filled PCF-based Michelson interferometer [60]. The cladding holes of the PCFs were filled liquid with an RI of 1.45. The voids of the PCF were collapsed fully in the splicing process and the collapsed region between SMF and PCF was about 300 μm . The PCF end face acted as the reflective surface for the core mode and cladding modes of the PCF, which were combined and interfered in the collapsed region at the return path. The device demonstrated high temperature sensitivity with the wavelength shifts being around 27 nm for a temperature change of 5°C [60].

Because PCF-based interferometers possess several desirable advantages including high sensitivity, linear response, and small size, they have attracted great interest in biosensing applications. Gao et al. proposed an in-line PCF Michelson interferometer for label-free, real time and sensitive detection of DNA hybridization and methylation [61]. To fabricate the interferometer,

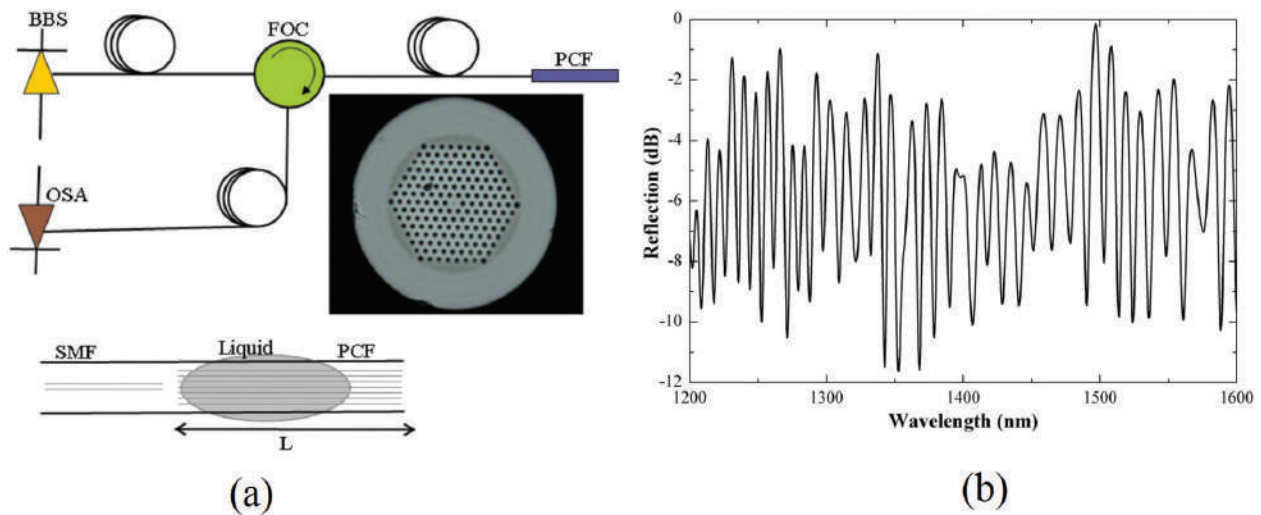


Figure 6. (a). Schematic of the experimental setup. A micrograph of the PCF used in the experiments is shown. The bottom drawing represents the interferometer, being L the length of the PCF. BBS stands for broad band source, FOC for fiber optic circulator or coupler, and OSA for optical spectrum analyzer. (b). Reflection spectrum of a device with $L = 24$ mm over 400 nm. Reprinted from Ref. [58], with the permission of AIP publishing.

a section of the PCF was collapsed to excite cladding modes which possessed lower effective refractive indices than that of the core mode. The end facet of the PCF was coated with a gold film as the reflective mirror. The DNA hybridization and methylation resulted in a variation of surrounding RI, which changed the effective refractive indices of the cladding modes. The experimental results demonstrated a detection limit of 5 nM [61].

Sun et al. demonstrated a hybrid fiber interferometer by splicing a short length of PM-PCF, 177 μm , to a SMF of one output port of a 2×2 50:50 fiber coupler, forming a Fabry-Perot cavity in one of the optical paths of the Michelson interferometer. The spectral response of the hybrid interferometer exhibited two distinctive interference fringes and was demonstrated experimentally for simultaneous measurements of ambient RI from 1.33 to 1.38 with a resolution of 8.7×10^{-4} , and temperature in the range of 35–500°C with sensitivity of 13 pm/°C [53].

Multicore fiber (MCF) based multipath Michelson interferometers have been proposed and demonstrated for high temperature sensing recently [64]. The reflective mirror was formed via arc-fusion splicing the fiber end face. The splicing region between SMF and MCF was tapered for coupling the center core mode to surrounding cores due to reduced distances. The seven cores acted as the different optical paths in the multipath Michelson interferometer. The device demonstrated a temperature sensitivity of 165 pm/°C in the temperature range of 250–900°C [64].

Besides sensor applications, generation of logic gates such as optical add-drop multiplexers based on PCF-based Michelson interferometers has been investigated recently [54].

2.4. Sagnac interferometer

Optical fiber Sagnac interferometers (OFSI) use a Sagnac loop as the sensing element which usually uses highly birefringent (Hi-Bi) fibers or polarization-maintaining fibers (PMFs) to introduce a large optical path difference for interference between two counter-propagating waves.

The configuration of a fiber Sagnac interferometer is illustrated by **Figure 7**. The input light is split by an optical fiber coupler, usually a 3 dB coupler. Two counter-propagating waves travel in the Sagnac loop and accumulate an optical path difference due to birefringence.

Compared to conventional Hi-Bi fibers, PM-PCFs usually achieve much higher birefringence. Consequently, the required length of PM-PCF in the Sagnac loop is much shorter than that of conventional PMFs. Moreover, PM-PCFs are thermally stable due to their pure-silica material used in the fiber compared to conventional PMFs with temperature dependent birefringence. PM-PCFs also possess advantage of low bending loss due to high numerical aperture and small core diameters. As a result, PM-PCF based Sagnac interferometers have been extensively exploited and develop for many applications, such as strain, twist, pressure and curvature sensing, etc.

The temperature insensitivity of PM-PCF based Sagnac interferometers improves the accuracy of strain measurements, as the temperature crosstalk is negligible. The temperature dependence of birefringence in the PM-PCF is 35 times smaller than that of conventional PMFs [65].

Further reduced temperature sensitivities in strain measurements using PM-PCFs were reported to be 0.29 pm/K, about 3000 times lower than that of conventional PMFs, with strain sensitivity of 0.23 pm/ $\mu\epsilon$ [66]. The experimental setup is shown in **Figure 8(a)**, consisting of a 3 dB fiber coupler to equally split the input light into two counter-propagating waves. The 86 mm long

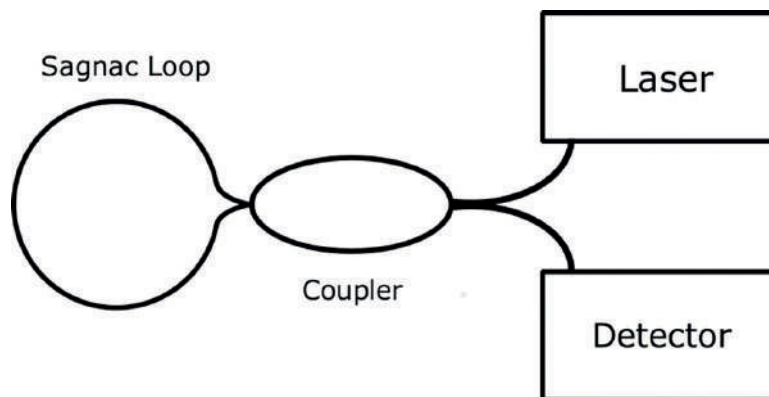


Figure 7. The schematic of a fiber Sagnac interferometer.

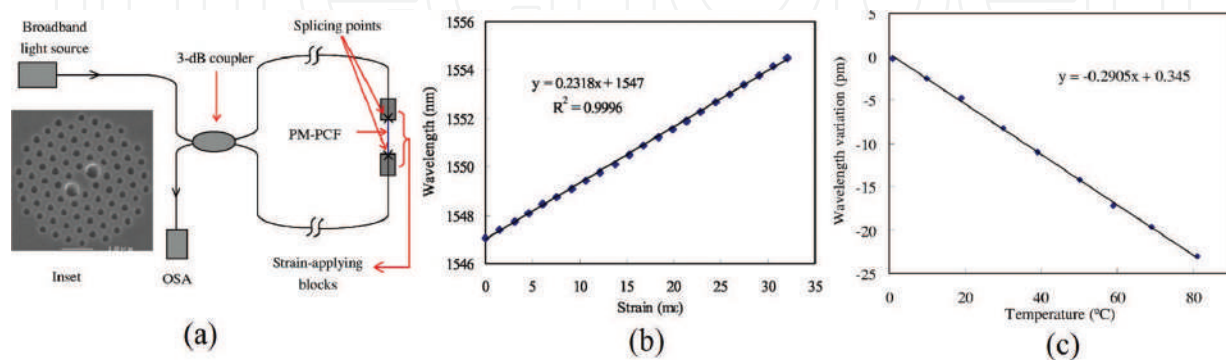


Figure 8. (a) Schematic diagram of the proposed OFSI strain sensor. Inset: SEM of the cross section of the PM-PCF. (b) wavelength shift of the transmission minimum at 1547 nm against the applied strain. (c) Wavelength variation of the transmission minimum at 1547 nm against temperature. Reprinted from Ref. [66], with the permission of AIP Publishing.

PM-PCF was spliced to the single mode fiber in the Sagnac loop. One end of the PM-PCF was fixed and the other end was stretched using a precision translation stage, for strain measurement. The scanning electron microscopic (SEM) image of the PM-PCF is shown in the inset of **Figure 8(a)**. A broadband light source is connected to the input port of the 3 dB coupler, and the transmitted light is measured by an optical spectrum analyzer (OSA) that is connected to the other input port of the 3 dB coupler. The interference occurred when two orthogonal guided modes combined at the coupler due to an accumulated phase delay in the Sagnac loop.

The transmission ratio of the optical intensity in the Sagnac loop can be described as:

$$T = [1 - \cos(\psi)]/2 \quad (5)$$

where $\psi = 2\pi LB/\lambda$ is the phase difference between the two orthogonal guided modes in PM-PCF, L is the length of the PM-PCF, B is the birefringence of the PM-PCF, and λ is the wavelength. The peak wavelength of the interference would encounter a shift due to the strain experienced by the PM-PCF, with the relationship being:

$$\Delta\lambda = \lambda(1 + p'_e)\varepsilon \quad (6)$$

where p'_e is a constant that describes the variation of strain-induced birefringence, and ε is the applied strain.

The linear relationship between strain and peak wavelength shift can be observed in **Figure 8(b)**. The temperature stability was tested by placing the PM-PCF in a temperature-controlled container, and the transmission spectrum was monitored by varying the temperature. The temperature sensitivity of the sensor was measured to be $-0.29 \text{ pm}/^\circ\text{C}$, as shown in **Figure 8(c)**, which is much lower than the reported value of $0.99 \text{ nm}/^\circ\text{C}$ of a conventional optical fiber Sagnac interferometer [67].

The influence of the coating on the fiber was investigated by Frazão et al., showing higher strain sensitivities and stronger temperature crosstalk with a nonlinear response for coated PCFs based Sagnac interferometers [68, 69]. The strain measurement sensitivities using PM-PCFs is also influenced by the ratio of the sensing PM-PCF over the entire PM-PCF length in the Sagnac loop [70]. Kim et al. develop a hollow core with an elliptical shape PBG fiber Sagnac interferometer for strain sensing with reduced temperature sensitivity when compared to conventional PMF Sagnac interferometers [71]. All-solid PCFs with Ge:SiO₂ rods and stress-induced birefringence by two Boron-doped rods have been reported to produce higher strain sensitivity of $25.6 \text{ pm}/\mu\varepsilon$ with the temperature crosstalk suppressed to $-9 \text{ pm}/\text{K}$ using a cascaded Sagnac configuration [72]. The reference signal at wavelength 1586.7 nm was used for temperature compensation of the two sensing wavelengths at 1551.5 nm and 1616.3 nm, with the wavelength difference being monitored [72]. Low-birefringence (low-Bi) PCFs with birefringence one or two orders lower than PM-PCFs were also exploited to achieve broader strain sensing range with similar strain sensitivity and a need for temperature compensation due to higher temperature sensitivity [73].

PCF-based Sagnac interferometers have been reported to develop twist or torsion sensors with potential applications in spaceflight and constructional engineering. Compared to other

optical fiber twist/torsion sensors, PCF-based Sagnac interferometers exhibit higher sensitivities and reduced crosstalk due to temperature. Hi-Bi PCFs have been reported to construct twist/torsion sensors with sensitivities 0.059 and 0.057 nm/°, as measured from two interference peaks, and temperature crosstalk of -4.6 and -2.6 pm/°C, respectively [74]. Improved twist sensitivities were obtained by using a low-Bi PCF Sagnac interferometer showing sensitivity of 1.00 nm/° and temperature sensitivity of -0.5 pm/°C [75]. A Side-leakage PCF with Ge-doped core based Sagnac interferometer was reported to achieve torsion sensitivity of 0.9354 nm/°. The temperature crosstalk was around 0.054–0.178 °/°C, which could be independently determined by using matrix method [76]. Notably, matrix method was used for simultaneously multi-parameter measurement by PCF base Sagnac interferometers also. Dong et al. introduced a core-offset technique in the splicing between the PCF and standard fibers in the Sagnac loop, and measured the wavelength variation and the transmissivity difference in order to demodulate the strain and temperature [77]. More recently, Naeem et al. demonstrated a Sagnac interferometer using Hi-Bi PCF for multi-parameter measurements. The sensor consisted of hybrid interferometry; the intra-core-mode Sagnac interference and the inter-core-mode Mach-Zehnder interference. The phase shifts due to the Sagnac and Mach-Zehnder interference were measured and used to construct the sensor matrix for torsion, strain and temperature [78].

Pressure sensing using PM-PCF based Sagnac interferometers have been reported recently. Due to the high sensitivity of Sagnac interferometry, such sensors do not require modifications for sensitivity enhancement. Furthermore, the detection scheme can be wavelength shift measurement [79, 80, 81], or phase shift measurement for extended pressure measurement range up to 2.35 MPa [82]. Feng et al. demonstrated that such sensors exhibit a good linearity of the applied pressure and can accurately measure pore water pressure [81].

Gong et al. employed a low-Bi PCF in the Sagnac loop and used wavelength shift detection for curvature sensing. The achieved curvature detection resolution was 0.059 m⁻¹ [83]. Comparatively, Frazão et al. demonstrated a Hi-Bi PCF Sagnac interferometer for curvature sensing with an improved detection resolution of $(1.39 \pm 0.07) \times 10^{-5}$ m⁻¹. The measurement parameter was the group birefringence β , which was defined as $\beta = \lambda^2 / \Delta\lambda L$, where λ is the central wavelength in operation, $\Delta\lambda$ is the spectral width of the interferometer, and L is the length of the Hi-Bi PCF region [84].

The presence of air holes in PCF structures permits the infiltration of substances, e.g. liquid, metal etc., to introduce additional functionalities. For instance, highly sensitive temperature sensing was reported by PCF based Sagnac interferometers filled with metal [85], selectively filled with liquid [86, 87], and partially filled with alcohol [88]. The indium-filled side hole PCF was producing a change in birefringence due to the expansion of the filler metal, resulting in a high temperature sensitivity of the sensor of -9.0 nm/°C [85]. A PBG PCF was selectively filled by high index liquid, leading to temperature dependence in the bandgap properties, as well as the Sagnac interference properties. The temperature sensitivity was about -0.4 nm/°C [88]. By selectively infiltrating water at the two larger air holes adjacent to the solid core in the PM-PCF, the Sagnac interferometer showed temperature sensitivity of 0.15 nm/°C [87]. In order to realize a low cost, reusable and reliable in-line microfluidic refractometer, Wu et al. devised a device

based on a C-shaped fiber and PCF based Sagnac interferometer [89]. The C-shape fiber and the PCF were fusion spliced to standard fibers in the Sagnac loop. The C-shape fibers provided openings for fluid to flow into and out of the PCF. The device was experimentally demonstrated for in-line fluid sensing, with high sensitivity of 6621 nm/RIU over RI range of 1.33–1.333 [89].

3. Conclusions and outlook

An overview of the different interferometric sensors, based on PCF, and their applications has been presented. The structure of PCFs is versatile and many different configurations can be achieved to produce interferometers with desirable properties such as high sensitivity, small sensor heads and good stability over time for sensing applications. PCF-based Fabry-Perot interferometers utilizing short sections of hollow core fibers, or forming microbubbles as the resonance cavities, or short sections of solid core PCFs, have been reported for measurements of various physical magnitudes, including RI, temperature, strain and pressure. PCF-based MZI configurations leverage on the enhanced flexibility in controlling waveguide properties in PCF, e.g. splicing between SMF and PCF can be used as an effective way to excite higher order modes and cladding modes in PCF, which exhibit greater sensitivity to ambient parameters compared to those in conventional fibers. In addition, the difference in the effective mode indices between the cladding modes and the core mode are greater in PCF, leading to much shorter device length and thus better robustness. PCF-based Michelson interferometers are a similar version of MZI configurations, except the presence of a reflective surface to reflect the modes which are combined at the same location of mode splitting. PCF-based Sagnac interferometers usually use Hi-Bi PCFs for developing compact and highly sensitive devices for measuring parameters such as strain, twist/torsion, curvature etc. PCFs can be combined with other fiber devices such as fiber Bragg grating or long period grating devices to achieve better sensor performance, e.g. higher sensitivity, minimizing cross-talk and simultaneous multiple parameter sensing. Inclusions of other substances into the holey structure of PCFs, bring additional functionalities and enhanced sensor performance such as temperature sensors. Moving forward, PCFs are expected for more exploitations and advancement of sensor development for various sensing applications.

Author details

Dora Juan Juan Hu^{1*}, Rebecca Yen-Ni Wong¹ and Perry Ping Shum^{2,3}

*Address all correspondence to: jjhu@i2r.a-star.edu.sg

1 Smart Energy and Environment Cluster, Institute for Infocomm Research, A*STAR, Singapore

2 Centre for Optical Fibre Technology, School of Electrical & Electronic Engineering, Nanyang Technological University, Singapore

3 CINTRA CNRS/NTU/THALES, UMI 3288, Research Techno Plaza, Singapore

References

- [1] Lee BH, Kim YH, Park KS, Eom JB, Kim MJ, Rho BS, et al. Interferometric fiber optic sensors. *Sensors*. 2012;**12**(3):2467-2486. DOI: 10.3390/s120302467
- [2] Knight JC. Photonic crystal fibres. *Nature*. 2003;**424**:847-851. DOI: 10.1038/nature01940
- [3] Tian F, Sukhishvili S, Photonic Crystal DH. Fiber as a lab-in-fiber optofluidic platform. In: Cusano A, Consales M, Crescitelli A, Ricciardi A, editors. *Lab-on-Fiber Technology*. Springer International Publishing; Switzerland, 2014. p. 315-334. DOI: 10.1007/978-3-319-06998-2_15
- [4] DJJ H, Ho HP. Recent advances in plasmonic photonic crystal fibers: Design, fabrication and applications. *Advances in Optics and Photonics*. 2017;**9**(2):257-314. DOI: 10.1364/AOP.9.000257
- [5] Villatoro J, Zubia J. New perspectives in photonic crystal fibre sensors. *Optics & Laser Technology*. 2016;**78**(A):67-75. DOI: 10.1016/j.optlastec.2015.07.025
- [6] Hu DJJ, Wang Y, Lim JL, Zhang T, Milenko KB, Chen Z, et al. Novel miniaturized Fabry–Perot refractometer based on a simplified hollow-core fiber with a hollow silica sphere tip. *IEEE Sensors Journal*. 2012;**12**(5):1239-1245. DOI: 10.1109/JSEN.2011.2167678
- [7] Rao YJ, Zhu T, Yang XC, Duan DW. In-line fiber-optic etalon formed by hollow-core photonic crystal fiber. *Optics Letters*. 2007;**32**(18):2662-2664. DOI: 10.1364/OL.32.002662
- [8] Villatoro J, Finazzi V, Coviello G, Pruneri V. Photonic-crystal-fiber-enables micro-Fabry-Perot interferometer. *Optics Letters*. 2009;**34**(16):2441-2443. DOI: 10.1364/OL.34.002441
- [9] Favero FC, Bouwmans G, Finazzi V, Villatoro J, Pruneri V. Fabry–Perot interferometers built by photonic crystal fiber pressurization during fusion splicing. *Optics Letters*. 2011;**36**(21):4191-4193. DOI: 10.1364/OL.36.004191
- [10] Wang Y, WD N, LC R, Hu T, Guo J, Wei H. Temperature-insensitive refractive index sensing by use of micro Fabry–Pérot cavity based on simplified hollow-core photonic crystal fiber. *Optics Letters*. 2013;**38**(3):269-271. DOI: 10.1364/OL.38.000269
- [11] Deng M, Tang CP, Zhu T, Rao YJ, LC X, Han M. Refractive index measurement using photonic crystal fiber-based Fabry-Perot interferometer. *Applied Optics*. 2010;**49**(9):1593-1598. DOI: 10.1364/AO.49.001593
- [12] Dash JN, Jha R. Fabry–Perot based strain insensitive photonic crystal fiber modal interferometer for inline sensing of refractive index and temperature. *Applied Optics*. 2015;**54**(35):10479-10486. DOI: 10.1364/AO.54.010479
- [13] Favero FC, Araujo L, Bouwmans G, Finazzi V, Villatoro J, Pruneri V. Spheroidal Fabry-Perot microcavities in optical fibers for high-sensitivity sensing. *Optics Express*. 2012;**20**(7):7112-7118. DOI: 10.1364/OE.20.007112
- [14] Ran ZL, Rao YJ, Deng HY, Liao X. Miniature in-line photonic crystal fiber etalon fabricated by 157 nm laser micromachining. *Optics Letters*. 2007;**32**(21):3071-3073. DOI: 10.1364/OL.32.003071

- [15] Shi Q, Wang Z, Jin L, Li Y, Zhang H, Lu F, et al. A hollow-core photonic crystal fiber cavity based multiplexed Fabry–Pérot interferometric strain sensor system. *IEEE Photonics Technology Letters*. 2008;**20**(15):1329-1331. DOI: 10.1109/LPT.2008.926948
- [16] Choi HY, Park KS, Park SJ, Paek UC, Lee BH, Cho ES. Miniature fiber-optic high temperature sensor based on a hybrid structured Fabry–Perot interferometer. *Optics Letters*. 2008;**33**(21):2455-2457. DOI: 10.1364/OL.33.002455
- [17] Du Y, Qiao X, Rong Q, Yang H, Feng D, Wang R, et al. A miniature Fabry–Pérot interferometer for high temperature measurement using a double-Core photonic crystal fiber. *IEEE Sensors Journal*. 2014;**14**(4):1069-1073. DOI: 10.1109/JSEN.2013.2286699
- [18] Frazão O, Aref SH, Baptista JM, Santos JL, Latifi H, Fahari F, et al. Fabry–Pérot cavity based on a suspended-core fiber for strain and temperature measurement. *IEEE Photonics Technology Letters*. 2009;**21**(17):1229-1231. DOI: 10.1109/LPT.2009.2024645
- [19] Wu C, HY F, Qureshi KK, Guan BO, Tam HY. High-pressure and high-temperature characteristics of a Fabry–Perot interferometer based on photonic crystal fiber. *Optics Letters*. 2011;**36**(3):412-414. DOI: 10.1364/OL.36.000412
- [20] Chen X, Zhao D, Qiang Z, Lin G, Li H, Qiu Y, et al. Polarization-independent Fabry–Perot interferometer in a hole-type silicon photonic crystal. *Applied Optics*. 2010;**49**(30):5878-5881. DOI: 10.1364/AO.49.005878
- [21] Lim JL, DJJ H, Shum PP, Wang Y. Cascaded photonic crystal fiber interferometers for refractive index sensing. *IEEE Photonics Journal*. 2012;**4**(4):1163-1169. DOI: 10.1109/JPHOT.2012.2205911
- [22] Choi HY, Kim MJ, Lee BH. All-fiber Mach-Zehnder type interferometers formed in photonic crystal fiber. *Optics Express*. 2007;**15**(9):5711-5720. DOI: 10.1364/OE.15.005711
- [23] Wang JN, Tang JL. Photonic crystal fiber Mach-Zehnder interferometer for refractive index sensing. *Sensors*. 2012;**12**(3):2983-2995. DOI: 10.3390/s120302983
- [24] Villatoro J, Finazzi V, Badenes G, Pruneri V. Highly sensitive sensors based on photonic crystal fiber modal interferometers. *Journal of Sensors*. 2009;**2009**:1-11. DOI: 10.1155/2009/747803
- [25] Zheng J, Yan P, Yu Y, Ou Z, Wang J, Chen X, et al. Temperature and index insensitive strain sensor based on a photonic crystal fiber inline Mach–Zehnder interferometer. *Optics Communications*. 2013;**297**:7-11. DOI: 10.1016/j.optcom.2013.01.063
- [26] Zhao Y, Li XG, Cai L, Refractive YY. Index sensing based on photonic crystal fiber interferometer structure with up-tapered joints. *Sensors and Actuators B: Chemical*. 2015;**221**:406-410. DOI: 10.1016/j.snb.2015.06.148
- [27] Wang Q, Kong L, Dang Y, Xia F, Zhang Y, Zhao Y, et al. High sensitivity refractive index sensor based on splicing points tapered SMF-PCF-SMF structure Mach-Zehnder mode interferometer. *Sensors and Actuators B: Chemical*. 2016;**225**:213-220. DOI: 10.1016/j.snb.2015.11.047

- [28] Wu D, Zhao Y, Li J. PCF taper-based Mach–Zehnder interferometer for refractive index sensing in a PDMS detection cell. *Sensors and Actuators B: Chemical*. 2015;**213**:1-4. DOI: 10.1016/j.snb.2015.02.080
- [29] Wong WC, Zhou W, Chan CC, Dong X, Leong KC. Cavity ringdown refractive index sensor using photonic crystal fiber interferometer. *Sensors and Actuators B: Chemical*. 2012;**161**(1):108-113. DOI: 10.1016/j.snb.2011.09.056
- [30] Liang H, Zhang W, Wang H, Geng P, Zhang S, Gao S, et al. Fiber in-line Mach–Zehnder interferometer based on near-elliptical core photonic crystal fiber for temperature and strain sensing. *Optics Letters*. 2013;**38**(20):4019-4021. DOI: 10.1364/OL.38.004019
- [31] Geng Y, Li X, Tan X, Deng Y, Hong X. Compact and ultrasensitive temperature sensor with a fully liquid-filled photonic crystal fiber Mach–Zehnder interferometer. *IEEE Sensors Journal*. 2014;**14**(1):167-170. DOI: 10.1109/JSEN.2013.2279537
- [32] Zhao Z, Tang M, Fu S, Liu S, Wei H, Cheng Y, et al. All-solid multi-core fiber-based multipath Mach–Zehnder interferometer for temperature sensing. *Applied Physics B*. 2013;**112**(4):491-497. DOI: 10.1007/s00340-013-5634-8
- [33] Qureshi KK, Liu Z, Tam HY, Zia MF. A strain sensor based on in-line fiber Mach–Zehnder interferometer in twin-core photonic crystal fiber. *Optics Communications*. 2013;**309**:68-70. DOI: 10.1016/j.optcom.2013.06.057
- [34] LM H, Chan CC, Dong XY, Wang YP, Zu P, Wong WC, et al. Photonic crystal fiber strain sensor based on modified Mach–Zehnder interferometer. *IEEE Photonics Journal*. 2012;**4**(1):114-118. DOI: 10.1109/JPHOT.2011.2180708
- [35] Shin W, Lee YL, BA Y, Noh YC, Ahn TJ. Highly sensitive strain and bending sensor based on in-line fiber Mach–Zehnder interferometer in solid core large mode area photonic crystal fiber. *Optics Communications*. 2010;**283**(10):2097-2101. DOI: 10.1016/j.optcom.2010.01.008
- [36] Kim B, Kim TH, Cui L, Chung Y. Twin core photonic crystal fiber for in-line Mach–Zehnder interferometric sensing applications. *Optics Express*. 2009;**17**(18):15502-15507. DOI: 10.1364/OE.17.015502
- [37] Sun B, Huang V, Liu S, Wang C, He J, Liao C, et al. Asymmetrical in-fiber Mach-Zehnder interferometer for curvature measurement. *Optics Express*. 2015;**23**(11):14596-14602. DOI: 10.1364/OE.23.014596
- [38] Deng M, Tang CP, Zhu T, Rao YJ. Highly sensitive bend sensor based on Mach–Zehnder interferometer using photonic crystal fiber. *Optics Communications*. 2011;**284**(12):2849-2853. DOI: 10.1016/j.optcom.2011.02.061
- [39] Tao C, Wei H, Feng W. Photonic crystal fiber in-line Mach-Zehnder interferometer for explosive detection. *Optics Express*. 2016;**24**(3):2806-2817. DOI: 10.1364/OE.24.002806
- [40] Lopez-Torres D, Elosua C, Villatoro J, Zubia J, Rothhardt M, Schuster K, et al. Photonic crystal fiber interferometer coated with a PAH/PAA nanolayer as humidity sensor. *Sensors and Actuators B: Chemical*. 2017;**242**:1065-1072. DOI: 10.1016/j.snb.2016.09.144

- [41] Hu P, Dong X, Wong WC, Chen LH, Ni K, CC C. Photonic crystal fiber interferometric pH sensor based on polyvinyl alcohol/polyacrylic acid hydrogel coating. *Applied Optics*. 2015;**54**(10):2647-2652. DOI: 10.1364/AO.54.002647
- [42] Dash JN, Jha R, Temperature Insensitive PCF. Interferometer coated with graphene oxide tip sensor. *IEEE Photonics Technology Letters*. 2016;**28**(9):1006-1009. DOI: 10.1109/LPT.2016.2522979
- [43] DJJ H, Lim JL, Park MK, Kao LTH, Wang Y, Wei H, et al. Photonic crystal fiber-based interferometric biosensor for streptavidin and biotin detection. *IEEE Journal of Selected Topics in Quantum Electronics*. 2012;**18**(4):1293-1297. DOI: 10.1109/JSTQE.2011.2169492
- [44] Lim JH, Jang HS, Lee K, KJ C, Lee BH. Mach-Zehnder interferometer formed in a photonic crystal fiber based on a pair of long-period fiber gratings. *Optics Letters*. 2004;**29**(4):346-348. DOI: 10.1364/OL.29.000346
- [45] Yu X, Shum P, Dong X. Photonic-crystal-fiber-based Mach-Zehnder interferometer using long-period gratings. *Microwave and Optical Technology Letters*. 2006;**48**(7):1379-1383. DOI: 10.1002/mop.21647
- [46] Choi HY, Park KS, Lee BH. Photonic crystal fiber interferometer composed of a long period fiber grating and one point collapsing of air holes. *Optics Letters*. 2008;**33**(8):812-814. DOI: 10.1364/OL.33.000812
- [47] Ju J, Jin W, Ho HL. Compact in-fiber interferometer formed by long-period gratings in photonic crystal fiber. *IEEE Photonics Technology Letters*. 2008;**20**(23):1899-1901. DOI: 10.1109/LPT.2008.2005207
- [48] Hu DJJ, Lim JL, Jiang M, Wang Y, Luan F, Shum PP, et al. Long period grating cascaded to photonic crystal fiber modal interferometer for simultaneous measurement of temperature and refractive index. *Optics Letters*. 2012;**37**(12):2283-2285. DOI: 10.1364/OL.37.002283
- [49] Pawar D, Rao CN, Choubey RK, Kale SN. Mach-Zehnder interferometric photonic crystal fiber for low acoustic frequency detections. *Applied Physics Letters*. 2016;**108**(4):041912-1-041912-4. DOI: 10.1063/1.4940983
- [50] Du J, Dai Y, Lei GKP, Tong W, Shu C. Photonic crystal fiber based Mach-Zehnder interferometer for DPSK signal demodulation. *Optics Express*. 2010;**18**(8):7917-7922. DOI: 10.1364/OE.18.007917
- [51] Gerosa RM, Spadoti DH, Menezes LS, de Matos CJS. In-fiber modal Mach-Zehnder interferometer based on the locally post-processed core of a photonic crystal fiber. *Optics Express* 2011;**19**(4):3124-3129. DOI: 10.1364/OE.19.003124
- [52] Tan X, Geng Y, Li X. High-birefringence photonic crystal fiber Michelson interferometer with cascaded fiber Bragg grating for pressure and temperature discrimination. *Optical Engineering*. 2016;**55**(9):090508. DOI: 10.1117/1.OE.55.9.090508

- [53] Sun H, Zhang J, Rong Q, Feng D, Du Y, Zhang X, et al. A hybrid fiber interferometer for simultaneous refractive index and temperature measurements based on Fabry–Perot/Michelson interference. *IEEE Sensors Journal*. 2013;**13**(5):2039-2044
- [54] Sousa JRR, Filho AFGF, Ferreira AC, Batista GS, Sobrinho CS, Bastos AM, et al. Generation of logic gates based on a photonic crystal fiber Michelson interferometer. *Optics Communications*. 2014;**322**:143-149. DOI: 10.1016/j.optcom.2014.02.023
- [55] Zhou A, Li G, Zhang Y, Wang Y, Guan C, Yang J, et al. Asymmetrical twin-Core fiber based Michelson interferometer for refractive index sensing. *Journal of Lightwave Technology*. 2011;**29**(19):2985-2991. DOI: 10.1109/JLT.2011.2165528
- [56] Chen NK, KY L, Shy JT, Lin C. Broadband micro-Michelson interferometer with multi-optical-path beating using a sphered-end hollow fiber. *Optics Letters*. 2011;**36**(11):2074-2076. DOI: 10.1364/OL.36.002074
- [57] Hu DJJ, Lim JL, Wang Y, Shum PP. Miniaturized photonic crystal fiber tip sensor for refractive index sensing. In: *Proceedings of the IEEE Sensors Conference; 28-31 October 2011; Limerick, Ireland: IEEE; 2011*. p. 1488-1490
- [58] Jha R, Villatoro J, Badenes G. Ultrastable in reflection photonic crystal fiber modal interferometer for accurate refractive index sensing. *Applied Physics Letters*. 2008;**93**(19):191106. DOI: 10.1063/1.3025576
- [59] Mileńko K, Hu DJJ, Shum PP, Zhang T, Lim JL, Wang Y, et al. Photonic crystal fiber tip interferometer for refractive index sensing. *Optics Letters*. 2012;**37**(8):1373-1375. DOI: 10.1364/OL.37.001373
- [60] Hsu JM, Horng JS, Hsu CL, Lee CL. Fiber-optic Michelson interferometer with high sensitivity based on a liquid-filled photonic crystal fiber. *Optics Communications*. 2014;**331**:348-352. DOI: 10.1016/j.optcom.2014.06.050
- [61] Gao R, DF L, Cheng J, Jiang Y, Jiang L, JD X, et al. Fiber optofluidic biosensor for the label-free detection of DNA hybridization and methylation based on an in-line tunable mode coupler. *Biosensors & Bioelectronics*. 2016;**86**:321-329. DOI: 10.1016/j.bios.2016.06.060
- [62] Gong H, Chan CC, Zhang YF, Wong WC, Dong X. Miniature refractometer based on modal interference in a hollow-core photonic crystal fiber with collapsed splicing. *Journal of Biomedical Optics*. 2011;**16**(1):017004. DOI: 10.1117/1.3527259
- [63] Li Z, Wang Y, Liao C, Liu S, Zhou J, Zhong X, et al. Temperature-insensitive refractive index sensor based on in-fiber Michelson interferometer. *Sensors and Actuators B: Chemical*. 2014;**199**:31-35. DOI: 10.1016/j.snb.2014.03.071
- [64] Duan L, Zhang P, Tang M, Wang R, Zhao Z, Fu S, et al. Heterogeneous all-solid multicore fiber based multipath Michelson interferometer for high temperature sensing. *Optics Express*. 2016;**24**(18):20210-20218. DOI: 10.1364/OE.24.020210

- [65] Kim DH, Kang JU. Sagnac loop interferometer based on polarization maintaining photonic crystal fiber with reduced temperature sensitivity. *Optics Express*. 2004;**12**(19):4490-4495. DOI: 10.1364/OPEX.12.004490
- [66] Dong X, Tam HY, Shum P. Temperature-insensitive strain sensor with polarization-maintaining photonic crystal fiber based Sagnac interferometer. *Applied Physics Letters*. 2007;**90**(15):151113. DOI: 10.1063/1.2722058
- [67] Starodumov AN, Zenteno LA, Monzon D, Rosa EDL. Fiber Sagnac interferometer temperature sensor. *Applied Physics Letters*. 1997;**70**(1):19. DOI: 10.1063/1.119290
- [68] Frazao O, Baptista JM, Santos JL. Temperature-independent strain sensor based on a Hi-Bi photonic crystal fiber loop mirror. *IEEE Sensors Journal*. 2007;**7**(10):1453-1455. DOI: 10.1109/JSEN.2007.904884
- [69] Frazao O, Baptista JM, Santos JL, Kobelke J, Schuster K. Strain and temperature characterisation of sensing head based on suspended-core fibre in Sagnac interferometer. *Electronics Letters*. 2008;**44**(25):1455-1456. DOI: 10.1049/el:20081431
- [70] Cui Y, Wu Z, Shum PP, Dinh XQ, Humbert G. Investigation on the impact of Hi-Bi fiber length on the sensitivity of Sagnac interferometer. *IEEE Sensors Journal*. 2014;**14**(6):1952-1956. DOI: 10.1109/JSEN.2014.2304521
- [71] Kim G, Cho T, Hwang K, Lee K, Lee KS, Han YG, et al. Strain and temperature sensitivities of an elliptical hollow-core photonic bandgap fiber based on Sagnac interferometer. *Optics Express*. 2009;**17**(4):2481-2486. DOI: 10.1364/OE.17.002481
- [72] Gu B, Yuan W, He S, Bang O. Temperature compensated strain sensor based on cascaded Sagnac interferometers and all-solid Birefringent hybrid photonic crystal fibers. *IEEE Sensors Journal*. 2012;**12**(6):1641-1646. DOI: 10.1109/JSEN.2011.2175725
- [73] Gong H, Chan CC, Chen L, Dong X. Strain sensor realized by using low-birefringence photonic-crystal-fiber-based Sagnac loop. *IEEE Photonics Technology Letters*. 2010;**22**(16):1238-1240. DOI: 10.1109/LPT.2010.2053025
- [74] Kim HM, Kim TH, Kim B, Chung Y. Temperature-insensitive torsion sensor with enhanced sensitivity by use of a highly birefringent photonic crystal fiber. *IEEE Photonics Technology Letters*. 2010;**22**(20):1539-1541. DOI: 10.1109/LPT.2010.2068043
- [75] Zu P, Chan CC, Jin Y, Gong T, Zhang Y, Chen LH, et al. A temperature-insensitive twist sensor by using low-birefringence photonic-crystal-fiber-based Sagnac interferometer. *IEEE Photonics Technology Letters*. 2011;**23**(13):920-922. DOI: 10.1109/LPT.2011.2143400
- [76] Chen W, Lou S, Wang L, Zou H, Lu W, Jian S. Highly sensitive torsion sensor based on Sagnac interferometer using side-leakage photonic crystal fiber. *IEEE Photonics Technology Letters*. 2011;**23**(21):1639-1641. DOI: 10.1109/LPT.2011.2166062
- [77] Dong B, Hao J, Chin-Yi L, Xu Z. Cladding-mode resonance in polarization-maintaining photonic-crystal-fiber-based Sagnac interferometer and its application for fiber sensor. *Journal of Lightwave Technology*. 2011;**29**(12):1759-1763. DOI: 10.1109/JLT.2011.2140313

- [78] Naeem K, Kim BH, Kim B, Chung Y. Simultaneous multi-parameter measurement using Sagnac loop hybrid interferometer based on a highly birefringent photonic crystal fiber with two asymmetric cores. *Optics Express*. 2015;**23**(3):3589-3601. DOI: 10.1364/OE.23.003589
- [79] HY F, Tam HY, Shao LY, Dong X, Wai PKA, Lu C, et al. Pressure sensor realized with polarization-maintaining photonic crystal fiber-based Sagnac interferometer. *Applied Optics*. 2005;**47**(15):2835-2839. DOI: 10.1364/AO.47.002835
- [80] HY F, Wu C, Tse MLV, Zhang L, Cheng KCD, Tam HY, et al. High pressure sensor based on photonic crystal fiber for downhole application. *Applied Optics*. 2010;**49**(14):2639-2643. DOI: 10.1364/AO.49.002639
- [81] Feng WQ, Liu ZY, Tam HY, Yin JH. The pore water pressure sensor based on Sagnac interferometer with polarization-maintaining photonic crystal fiber for the geotechnical engineering. *Measurement*. 2016;**90**:208-214. DOI: 10.1016/j.measurement.2016.04.067
- [82] Cho LH, Wu C, Lu C, Tam HY. A highly sensitive and low-cost Sagnac loop based pressure sensor. *IEEE Sensors Journal*. 2013;**13**(8):3073-3078. DOI: 10.1109/JSEN.2013.2261291
- [83] Gong HP, Chan CC, Zu P, Chen LH, Dong XY. Curvature measurement by using low-birefringence photonic crystal fiber based Sagnac loop. *Optics Communications*. 2010;**283**(16):3142-3144. DOI: 10.1016/j.optcom.2010.04.023
- [84] Frazão O, Baptista JM, Santos JL, Roy P. Curvature sensor using a highly birefringent photonic crystal fiber with two asymmetric hole regions in a Sagnac interferometer. *Applied Optics*. 2008;**47**(13):2520-2523. DOI: 10.1364/AO.47.002520
- [85] Reyes-Vera E, Cordeiro CMB, Torres P. Highly sensitive temperature sensor using a Sagnac loop interferometer based on a side-hole photonic crystal fiber filled with metal. *Applied Optics*. 2017;**56**(2):156-162. DOI: 10.1364/AO.56.000156
- [86] Zheng X, Yg L, Wang Z, Han T, Wei C, Chen J. Transmission and temperature sensing characteristics of a selectively liquid-filled photonic-bandgap-fiber-based Sagnac interferometer. *Applied Physics Letters*. 2012;**100**(14):141104. DOI: 10.1063/1.3699026
- [87] Cui Y, Shum PP, Hu DJJ, Wang G, Humbert G, Dinh XQ. Temperature sensor by using selectively filled photonic crystal fiber Sagnac interferometer. *IEEE Photonics Journal*. 2012;**4**(5):1801-1808. DOI: 10.1109/JPHOT.2012.2217945
- [88] Zhao CL, Wang Z, Zhang S, Li Q, Zhong C, Zhang Z, et al. Phenomenon in an alcohol not full-filled temperature sensor based on an optical fiber Sagnac interferometer. *Optics Letters*. 2012;**37**(22):4789-4791. DOI: 10.1364/OL.37.004789
- [89] Wu C, Tse MLV, Liu Z, Guan BO, Lu C, Tam HY. In-line microfluidic refractometer based on C-shaped fiber assisted photonic crystal fiber Sagnac interferometer. *Optics Letters*. 2013;**38**(17):3283-3286. DOI: 10.1364/OL.38.003283

We are IntechOpen, the world's leading publisher of Open Access books Built by scientists, for scientists

6,300

Open access books available

171,000

International authors and editors

190M

Downloads

Our authors are among the

154

Countries delivered to

TOP 1%

most cited scientists

12.2%

Contributors from top 500 universities



WEB OF SCIENCE™

Selection of our books indexed in the Book Citation Index
in Web of Science™ Core Collection (BKCI)

Interested in publishing with us?
Contact book.department@intechopen.com

Numbers displayed above are based on latest data collected.
For more information visit www.intechopen.com



Dual-Core Transversally Chirped Microstructured Optical Fiber for Mode-Converter Device and Sensing Application

Erick Reyes Vera, Juan Úsuga Restrepo,
Margarita Varon and Pedro Torres

Additional information is available at the end of the chapter

<http://dx.doi.org/10.5772/intechopen.70989>

Abstract

We propose and demonstrate the concept of transversally chirped microstructured optical fiber and its application for the development of new platforms for sensing and telecommunications devices. First, the feasibility of the structure is demonstrated through two different techniques of manufacture. Based on the proposed structure, a novel mode-converter device is numerically studied. It is found that the mode conversion between LP_{01} and LP_{11} modes can be continuously tuned by temperature changes from 25 to 75°C. And that, the coupling efficiency in the wavelength range between 1.2 μm and 1.7 μm is always higher than 65%. Consequently, the proposed mode converter can operate in the E + S + C + L + U bands. Finally, a similar structure was used to design a new sensing architecture, which consisting of a dual-core transversally chirped microstructured optical fiber for refractive index sensing of fluids. We show that by introducing a chirp in the hole size, the microstructured optical fiber can be a structure with decoupled cores, forming a Mach–Zehnder interferometer in which the analyte directly modulates the device transmittance by its differential influence on the effective refractive index of each core mode. We show that by filling all fiber holes with analyte, the sensing structure achieves high sensitivity (transmittance changes of 302.8 per RIU at 1.42) and has the potential for use over a wide range of analyte refractive index.

Keywords: microstructured optical fibers, fiber optics sensors, interferometry, mode converter, space, division multiplexing, refractive index sensor, mode conversion, Mach–Zehnder interferometer

1. Introduction

In the last two decades, several technological breakthroughs were needed to increase and satisfy the capacities of the optical links. Some important advances allow the connection between users through the implementation of optical fibers. One of the most important advances, related to these technological breakthroughs, is the use of broadband optical amplifiers to increase the length of optical links. On the other hand, different multiplexing techniques such as optical time division multiplexing (OTDM), wavelength division multiplexing (WDM) and polarization division multiplexing (PDM) have been implemented in transmission channels to increase the optical transmission system capacity. However, due the high growth in the demand, the transmission capacity of this technology has reached the limits imposed by the nonlinear effects in optical fiber [1, 2]. In order to keep up the growth of current optical communication networks, it is necessary to implement new technological breakthroughs. One possibility is the implementation of independent spatial channels to send information. This technique is known as spatial division multiplexing (SDM) and can be implemented in two different schemes. Intuitively, in the multi-core fiber (MCF) scheme, each core acts as an independent channel for sending the information [1], while in the modal division multiplexing (MDM) scheme, each mode is considered an independent transmission channel as in single-mode fiber [3, 4]; hence, the key is to convert the fundamental fiber modes to higher order modes. As the processing systems are not prepared to work with hundreds of modes, in the MDM scheme it is preferred to work with few modes fibers (FMFs) [3, 4]. As with any new technology, emerging SDM systems require the development of new components such as optical fibers that support multiple spatial modes and integrated mode converters to control propagating modes, spatial mode multiplexers (SMUXs) and demultiplexers (SDEMUXs).

To address these needs, several works have reported different mechanisms to control the propagation modes in FMFs, such as long period fiber grating (LPFG), Fiber Bragg Gratings (FBG), tapers and phase mask [5–10]. Another interesting alternative is to use microstructured optical fibers (MOFs), also called photonic crystal fibers (PCFs), which offer flexibility in its design and the possibility of manipulating the optical properties of the device because its characteristics—dispersion, effective area, birefringence and nonlinearity, among others—depends on the diameter of holes, the separation between them and the shape of the microstructure [11–17]. Owing these characteristics, these type of optical fibers have been employed for the development of different devices such as polarization beam splitters [18], dispersion compensators [19, 20] and mode converters [5] to name a few.

Mode selective couplers (MSC) based on microstructured optical fiber (MOF) represent one of the best approaches to achieve mode conversion, avoiding the problems of other techniques—bulky free-space optics, polished- and fused-type MSC—since the devices are compact, robust and efficient, and allows the possibility of manipulating its behavior based on the MOF geometrical parameters [3, 21–24]. The principle of MSC is to phase match the fundamental mode in a single-mode fiber with a high-order mode in FMF.

In [23], Cai et al. proposed a mode converter based on a hybrid dual-core MOF, which contains an index-guided core and a photonic bandgap core. The air holes of the first ring

around one of the cores are replaced with high-index rods, then mode conversions can be continuously achieved by varying the refractive index of high-index rods. The all-solid bandgap structure requires two suitable materials that are also compatible for drawing and splicing with few-mode fibers. In [24], the authors proposed a tuneable MSC based on a fully liquid-filled dual-core MOF with non-identical cores. The tuning of the wavelength in the S + C + L + U bands is performed by changing the refractive index (RI) of the filling fluid.

Simultaneously, the implementation of MOFs has allowed the development of a new family of optical fiber sensors, which present higher sensitivity and compact sizes compared to sensors based in standard optical fibers and other technologies [25]. Some novel configurations of these sensors have been implemented in the measurement of refractive index (RI) changes [26, 27], temperature [28, 29] and force [30–32], among others. The refractive index sensors are the most studied and applied in recent years in biological, medical and chemical applications [33–38]. Two general configurations for the interaction between the light and analyte in MOFs may be identified. In the first option, the analyte is located in the evanescent field of the waveguide [39, 40]. In the second option, the analyte can be inserted into the fiber holes and experience long range interaction with the guided light while maintaining the waveguide, thereby ensuring a robust device [26, 41]. In addition, optical fiber sensors based on the dual-core MOF configuration are able to achieve improved sensitivity for RI measurements. In these structures, the fiber holes are filled with the analyte. Then, the refractive index of the sample modulates the device transmittance by its influence on the coupling between the cores. In [37], Markos et al. presented an experimentally feasible design of a dual-core microstructured polymer optical fiber (mPOF), which can act as a label-free selective biosensor. Numerical results indicate a sensitivity of 20.3 nm/nm—wavelength shift per nm thickness of biolayer—achieved with a 15-cm-long device at visible region where the mPOF has the lowest absorbance. Recently, Wu et al. proposed and demonstrated a novel configuration with a sensitivity of 30,100 nm per refractive index unit (nm/RIU). This configuration is based on a directional coupler architecture using a solid-core PCF [42]. Yuan et al. demonstrated the design of an all-solid dual-core photonic bandgap fiber, in which a single hole between the cores acts as microfluidic channel for the analyte [43]. The predicted sensitivity was 70,000 nm/RIU. In 2011 [44], Sun et al. proposed and demonstrated a refractive index sensor based on the selectively resonant coupling between a conventional solid core and a microstructured core. Numerical results shown that this configuration could achieve a sensitivity of 8500 nm/RIU. However, these configurations have also some drawbacks, for instance, have complex design for the fiber cores or require selective filling. For this reason, the implementation of interferometric schemes in combination with these specialty fibers has emerged as a new alternative. In [26], we introduced the concept of transversally chirped solid-core MOF and reported a dual-core chirped MOF that could act as a structure with decoupled cores, thus forming a Mach-Zehnder interferometer in which the analyte directly modulated the device transmittance by its differential influence on the effective RI of each core mode, achieving a sensitivity of 300 per RIU for a 12-mm-long device and analyte RI of 1.42. A year later, we designed a label-free biosensor by immobilization of an antigen sensor layer onto the walls of the air holes of rings surrounding one core of the fiber. A sensitivity of around 3.7 nm/nm was achieved for a 10 mm

long device at near IR wavelengths [38]. Then, we studied some refractometric properties of these configuration using numerical models to improve the performance of this device [41].

The chirp concept has been widely used in one-dimensional structures such as chirped mirrors [45] and chirped fiber Bragg gratings where different spectral components are localized at different positions inside the chirped structure [46]. In both cases, the chirp was implemented on the propagation direction. Chirping also has already been applied for designing hollow core fibers with a radially chirped microstructured cladding [47]. By introducing a radial chirp into the photonic crystal structure, it was demonstrated a novel concept that breaks with the paradigm of lattice homogeneity and enables a new degree of freedom in the design of MOFs. Another important variation was reported by Ghosh et al. [48]. The authors proposed a novel chirped cladding as a novel tailoring tool to attain wider transmission window and reduced temporal dispersion in an all-solid Bragg-like MOF.

In this chapter, dual-core transversally chirped MOFs for active mode conversion in telecommunications and sensing applications are presented. In the first part of this chapter, we explain the fabrication process of this novel structure. Next, we demonstrate that this type of MOF can be used to design a novel and tuneable mode-converter to improve the performance of the modern optical systems. Finally, a dual-core transversally chirped MOF is proposed to create a compact highly sensitivity optical fiber sensor.

2. Fabrication methodology

Two techniques can be used to fabricate dual-core transversally chirped MOFs. The first alternative consists in the implementation of the standard stack and draw technique [49, 50]. The first step is producing the preform, which is based on stacking of capillaries and rods. In our case, the diameter of the capillary should have a slight reduction in its diameter along the cross-section. Then, several slightly chirped preforms of about 1 mm were obtained by pulling a ~ 1 cm preform with a small transversal temperature gradient. The temperature gradient was produced by pulling the preform off-center [26]. After this process the fiber shown in **Figure 1(a)** was obtained, which is characterized by a slight transverse chirp in the hole distribution.

The second alternative consists in tapering the MOF from the previous step, in such a way that fiber structures with a larger transverse chirp can be achieved. In our case, MOF tapers were produced by using the flame brushing technique. The MOF was mounted on a motorized stage. The fiber was heated using a butane flame, which was mounted on a second motorized stage. The butane flame was moved back and forth along the fiber axis as the taper was pulled simultaneously. In order to ensure that the holes do not collapse, it was applied pressure within the holes. **Figures 1(b)** and **(c)** show the cross-section of two tapered MOFs obtained with an applied pressure of 6 and 7 bars, respectively. From these results, it is evident that the pressure applied inside of fiber holes can control the transversal chirp of the pristine MOF. For example, the MOF with an applied pressure of 6 bars has a structure in which none

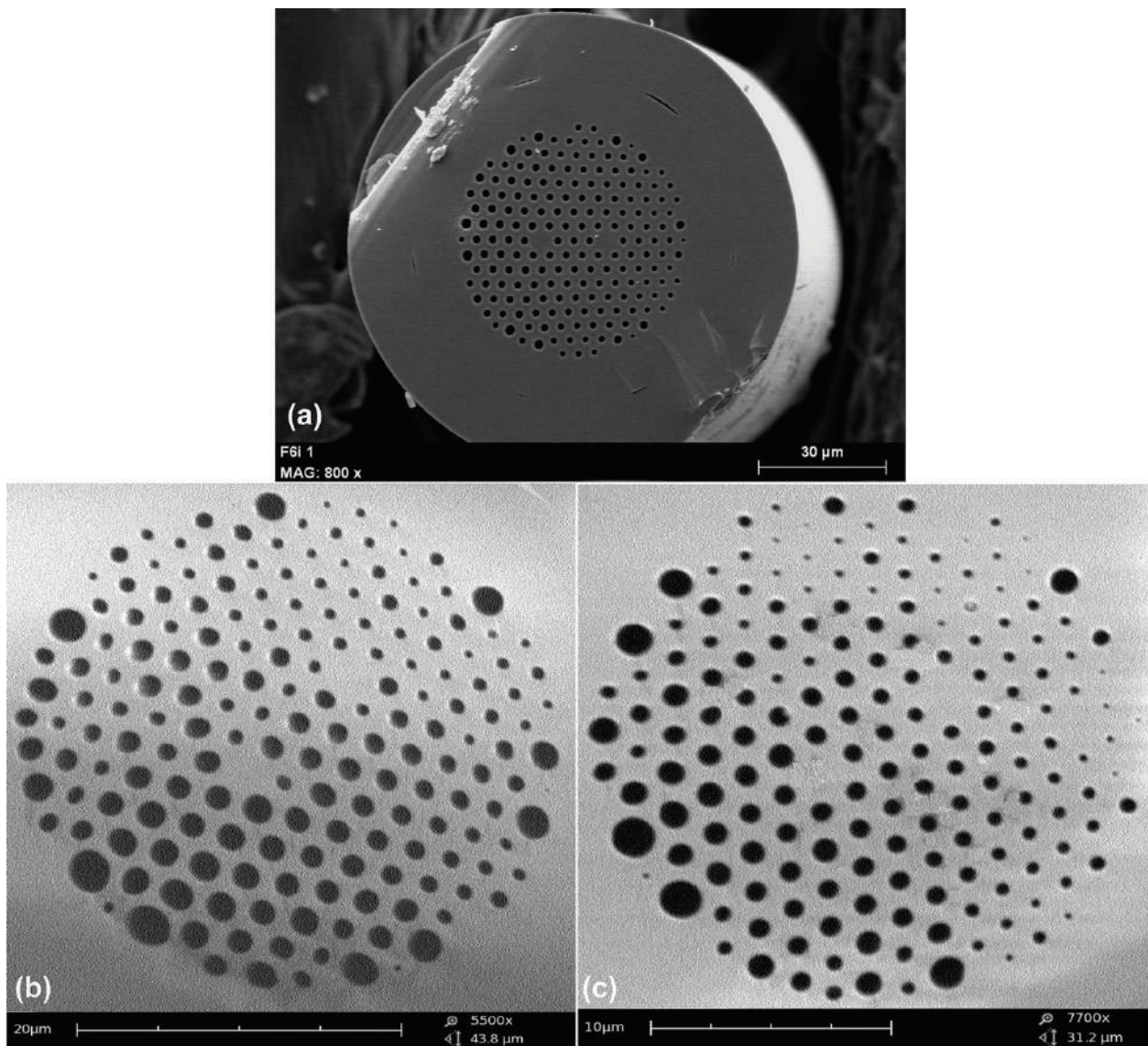


Figure 1. SEM images of (a) a dual-core transversally chirped MOF obtained with the standard stack and draw technique. (b) and (c) Dual-core transversally chirped MOF tapers obtained through the flame brushing technique at 6 and 7 bars, respectively, within the fiber holes.

of the holes collapsed during the tapering process and the transverse chirping slope is smaller than the MOF obtained when the pressure was 7 bars.

3. Mode converter device

The cross-section of the proposed dual-core transversally chirped MOF MSC is shown in **Figure 2**. As we can see, the cladding holes are arranged in a hexagonal lattice with constant pitch $\Lambda = 6 \mu\text{m}$. The diameter of the circular air holes decreases linearly from $d_{\text{max}} = 6 \mu\text{m}$ on the left side of the fiber to $d_{\text{min}} = 0.9 \mu\text{m}$ on the right side. The considered MOF has two solid

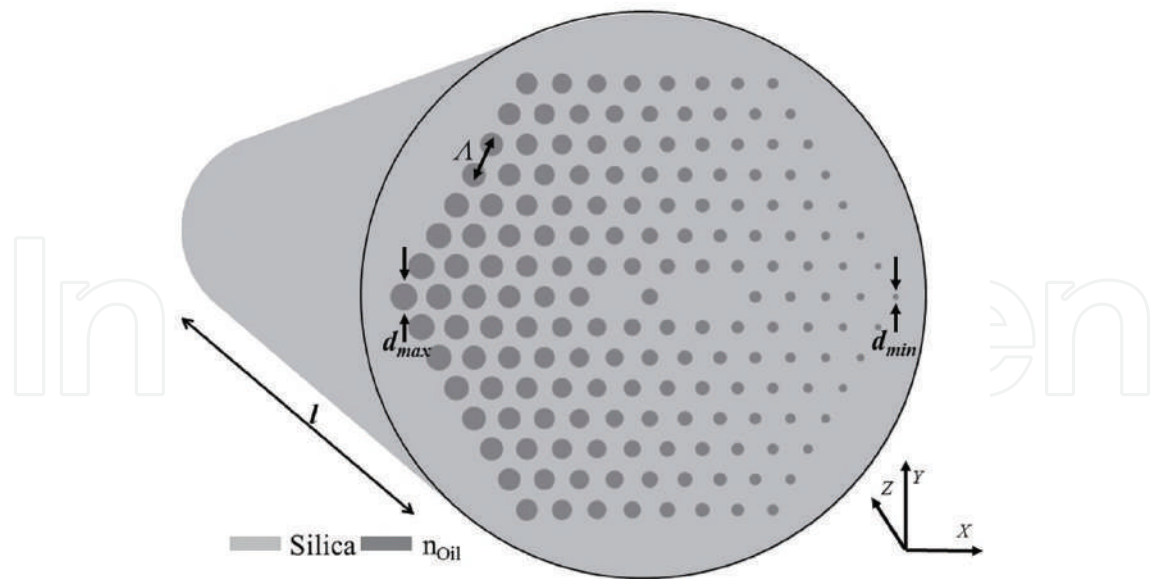


Figure 2. Structure of the mode selective coupler based on a dual-core transversally chirped MOF.

cores, which are separated by only one hole in the microstructure, that is, by 2Λ . In this case, we employ a small separation between both cores in order to guarantee power transfer. In addition, background material is silica, and its dispersion is given by Sellmeier's equation [51]. Note that by the transverse chirping of the microstructure, the fiber cores obviously do not have the same shape. In this case, the right core is almost 1.8 times wider than the left core.

In our device, a RI-matching oil (Cargille Labs., $n_0 = 1.42$ at room temperature) is chosen to be filled onto the MOF, and its thermo-optic coefficient is $\alpha = 3.94 \times 10^{-4}/\text{C}^\circ$, and the relationship between refractive index n and temperature T is to be $n = n_0 - \alpha(T - T_0)$ where T_0 is the room temperature. A variety of functional fiber devices have been fabricated based on MOF fully infiltrated by fluid such as optical switches [52, 53], all-optical modulator [54], tunable optical filters [55] and fiber polarimeters [56].

According to our design, the fundamental mode LP_{01} in the left core is converted to the LP_{11} mode in the right core. Because the right core supports two modes (LP_{01} and LP_{11}), supermode analysis [57] was used to investigate the behavior of the temperature-controlled mode converter. We performed finite element simulations under different temperature conditions at the particular free-space wavelength $\lambda = 1.55 \mu\text{m}$.

Figure 3 shows the effective index curves of symmetric (supermode 1) and antisymmetric (supermode 2) modes. From these results, it is evident that LP_{01} mode in the left core interacts with LP_{11} mode in the right core. As expected, the effective refractive index n_{eff} of both supermodes decrease with increasing temperature. In addition, the effective index of symmetric mode is always slightly larger than that of antisymmetric mode, indicating that these supermodes have different propagation constants and therefore there is a beating between these two modes and, thus, the power fluctuates back and forth between the two cores.

Once it was determined which modes exchange energy, the coupled mode theory was applied to find the phase-matching conditions [57, 58]. Here, each core is analyzed as an independent

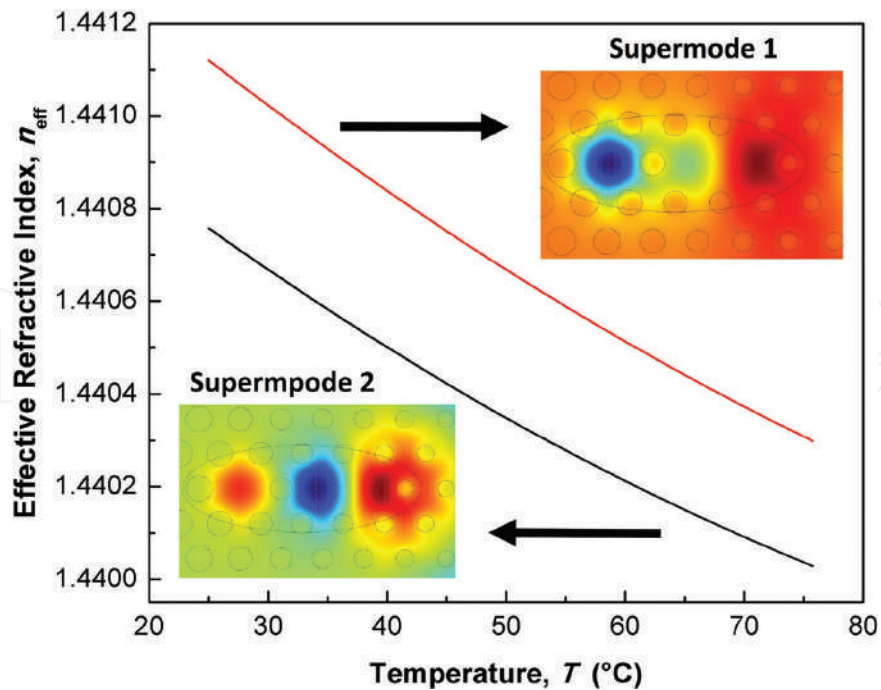


Figure 3. Supermode analysis of the dual core transversally chirped MOF when temperature varies from 25 to 75°C at an operating wavelength $\lambda=1.55 \mu\text{m}$.

waveguide to avoid the perturbations caused by the presence of the other core. When the mode of the left core interacts with the mode of the right core, crossing occurs and propagation constants of the two modes are matched. Then, maximum power transfer can be achieved at the phase-matching wavelength.

Figure 4(a) presents the modal dispersion curves of LP_{01} mode in the left core and of LP_{11} mode in the right core with different temperature values in the wavelength range 1.2–1.8 μm . Colored points in this figure represent the phase-matching wavelengths. **Figure 4(b)** shows the dependence of the operating wavelength on temperature. Therefore, the liquid-filling method is an easy method to tune the behavior of this device. According to this result, this mode converter could operate in the E + S + C + L + U bands.

To test the mode-conversion performance of the coupler, **Figure 5** presents the normalized power as a function of fiber length at a wavelength of 1.55 μm . It is observed that almost 100% of the power is coupled between the cores with the beating length $L_c = 2 \text{ mm}$. This result shows that the proposed device is compact compared with other MOF-based mode converters [5, 7, 23–25].

Finally, the mode coupling efficiency of the device was evaluated. The results are depicted in **Figure 6**. From these results, it is evident that the mode coupling efficiency obtained with this structure presents a good performance in the E + S + C + L + U bands. As expected, the behavior of this device can be thermally controlled. It is observed that the phase-matching wavelength varies with the temperature change. It is found that when T increases, the operating wavelength also increases. In addition, coupling efficiencies above 65% were obtained in this study.

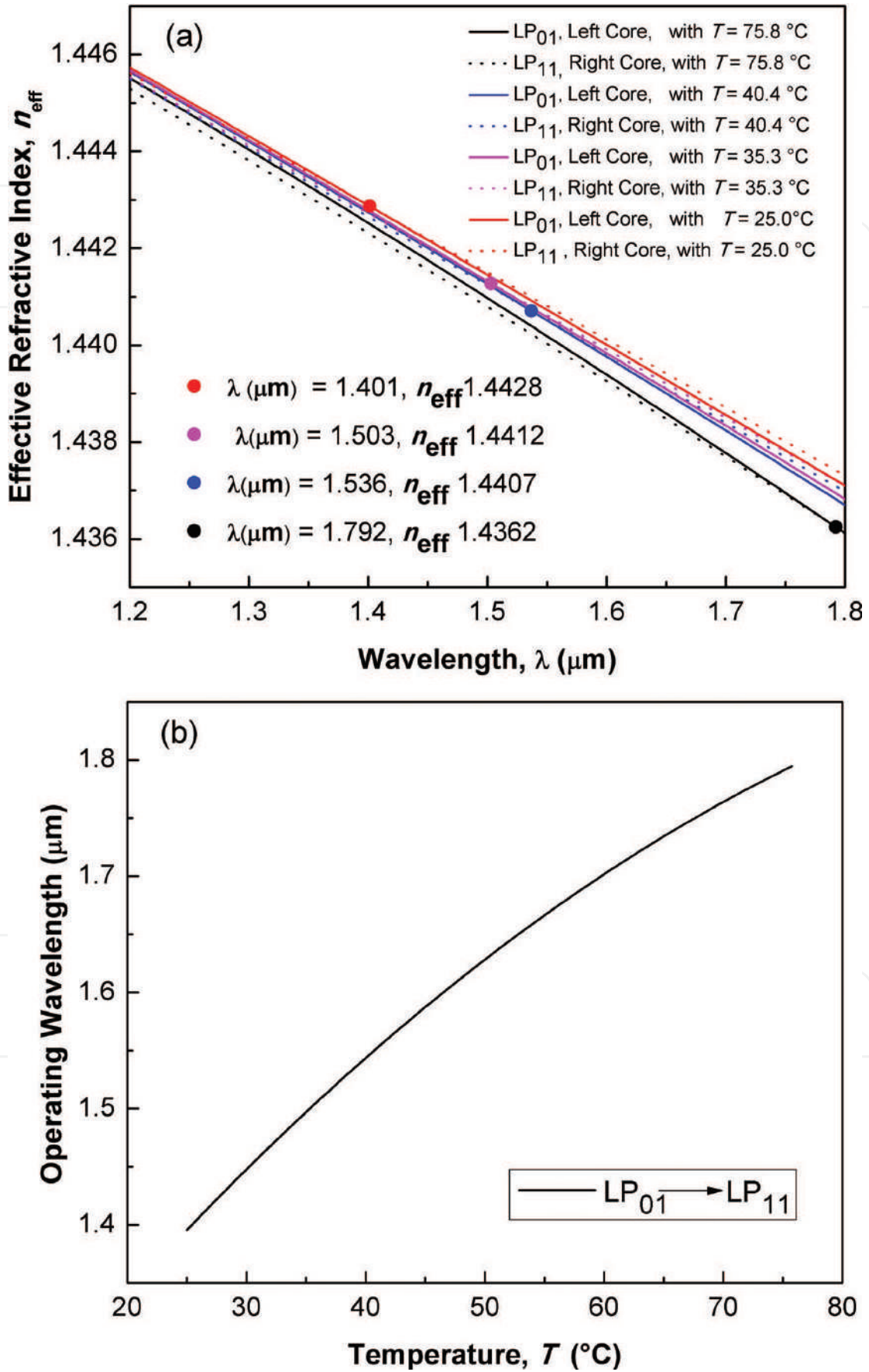


Figure 4. (a) Modal dispersion curves for LP₀₁ mode in the left core and LP₁₁ in the right core with temperature. (b) Operating wavelength as function of applied temperature on mode converter based on dual-core transversally chirped MOF.

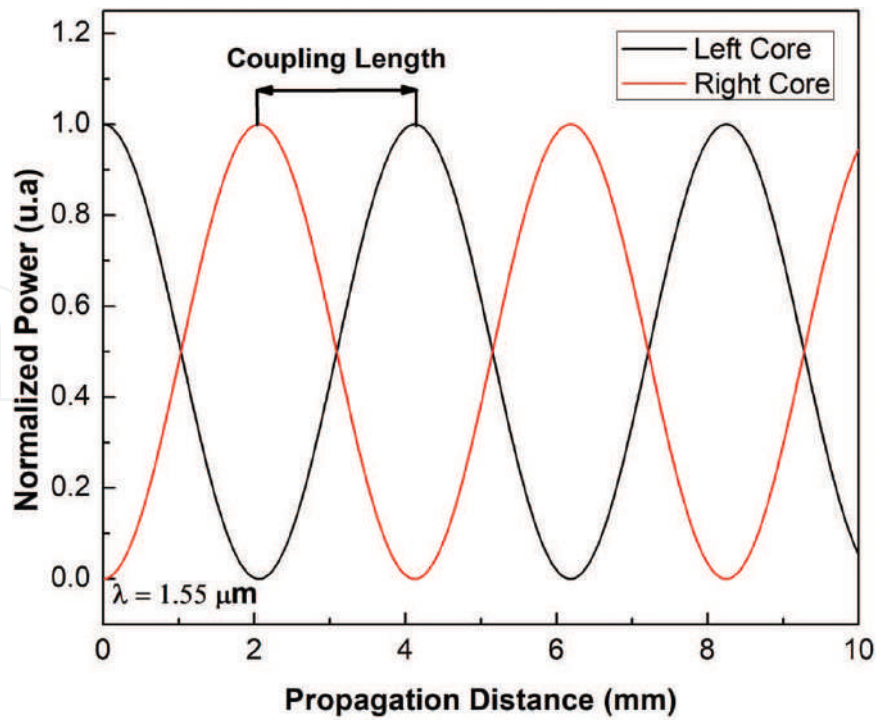


Figure 5. Normalized power transfer for the proposed mode-converter device with $T = 25^\circ\text{C}$.

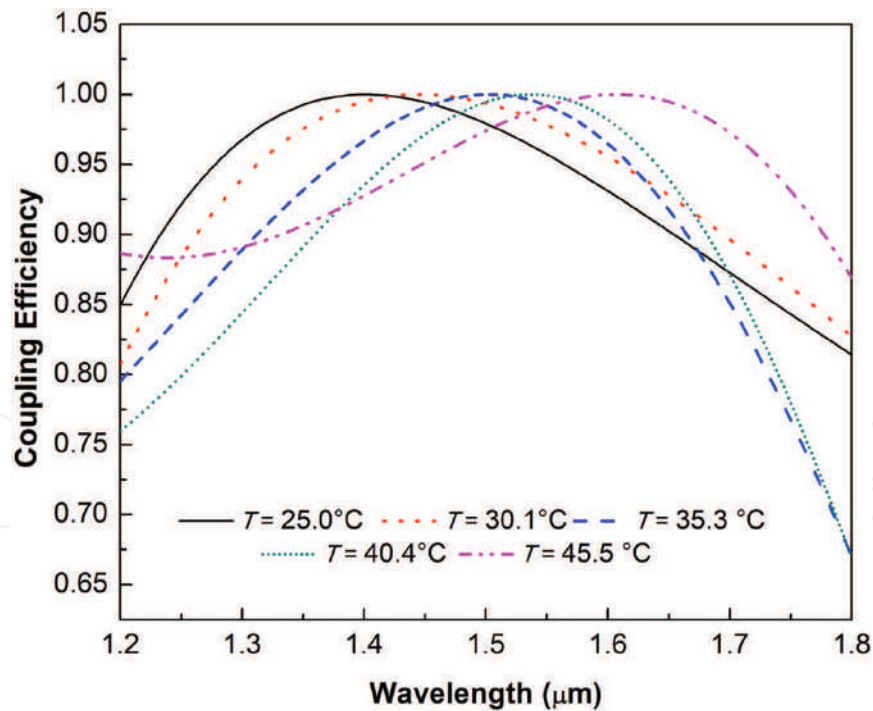


Figure 6. Comparison of mode coupling efficiency for different temperature values in the telecommunication windows.

4. Refractive index sensor

The dual-core transversally chirped MOF that is considered for refractive index sensing of fluids has a similar structure to the fibers in **Figures 1(b)** and **(c)**. Now, it is necessary to guarantee

that the cores are uncoupled to exploit the fiber as a Mach-Zehnder interferometer (MZI) [27]. Then, the distance between the cores is increased to 4Λ , where in this new design $\Lambda = 4.33 \mu\text{m}$. This separation was considered because small fluctuations in fiber diameter due to fabrication tolerances may affect the performance of the sensor. In this structure, the diameter of the air holes decreases linearly from $d_{\text{max}} = 2.6 \mu\text{m}$ to $d_{\text{min}} = 0.6 \mu\text{m}$, so the relative sizes of holes (d/Λ) range from 0.6 to 0.13 μm . As expected, the cores are non-identical because the holes around the right core are smaller than the holes around the left core. However, both cores are single-mode waveguides due to the slight chirp.

In addition, we consider as an example label-free antibody detection using the highly selective antigen-antibody binding based on our previous experience as another important variation [39]. Then, the first ring of air holes around the right core are functionalized for antibody detection by immobilization of an antigen sensor layer onto the walls of the holes as is shown in **Figure 7**. This layer can consist of a functionalization layer of a certain thickness in addition to the antigen layer. Then, we consider a layer with a thickness t_s equal to 40 nm for sensing the antibody α -streptavidin with thickness $t_a = 5 \text{ nm}$. The refractive index of the sensor layer and α -streptavidin is 1.45 (we neglect the dispersion of the biomolecule layer).

From **Figure 8** the operation of the sensor can be clearly understood. The refractometric sensor gains its sensitivity from the fact that only the mode of the right core has substantial overlap with the analyte. This arises because of the low fraction ratio (d/Λ) of holes that surrounding this core. Then the light is not well confined. Now, the RI of the analyte directly modulates the device transmittance by its differential influence on the effective refractive index of each core mode, resulting in a variable phase difference between the optical path lengths of the interferometer arms. Therefore, the proposed configuration was classified as a modal interferometer in the sense that two modes of the dual-core structure are interfering among them. Here, the performance of the sensor is compared with an interesting variation. It consists in

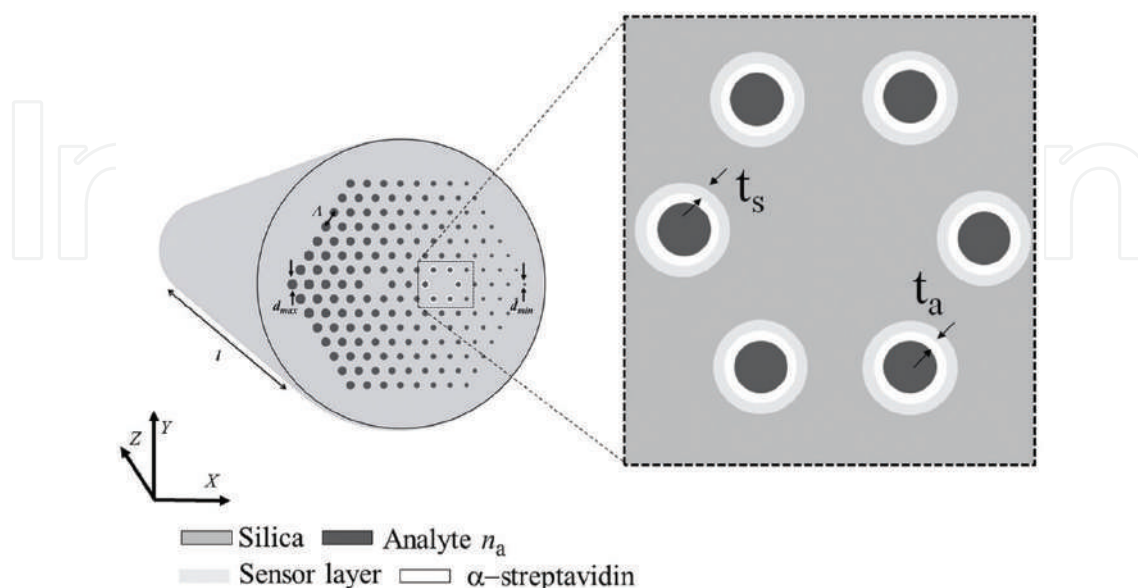


Figure 7. Dual-core transversally chirped MOF biosensor with $\Lambda = 4.33 \mu\text{m}$ and the hole diameter vary from $d_{\text{max}} = 2.6 \mu\text{m}$ to $d_{\text{min}} = 0.6 \mu\text{m}$. In this design, the fiber cores are uncoupled.

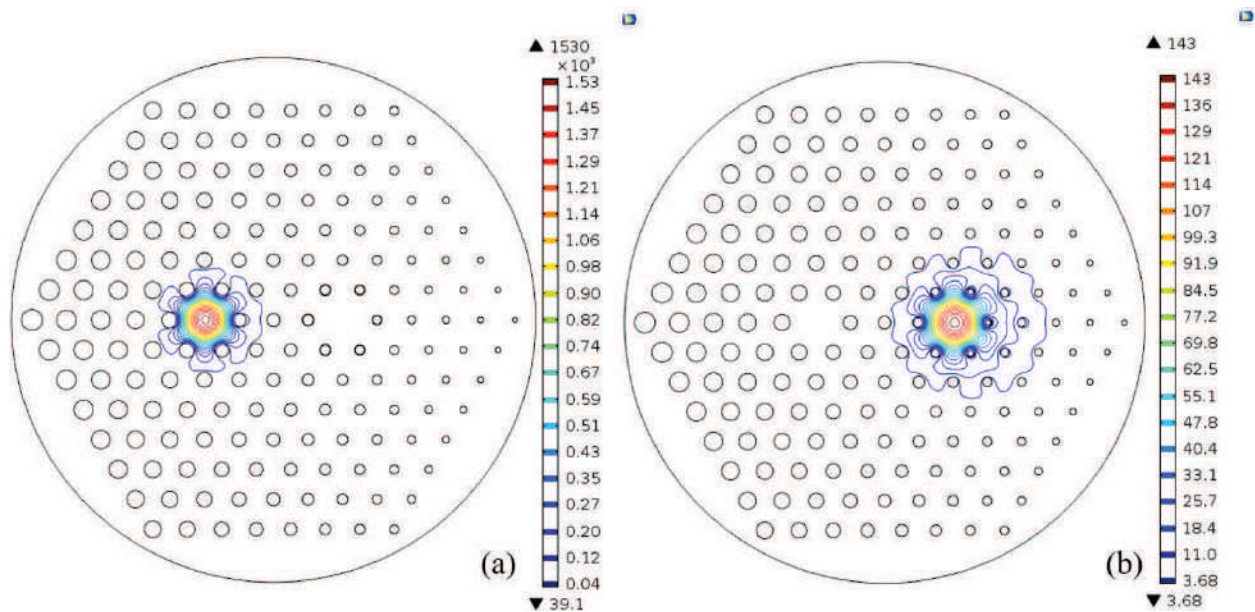


Figure 8. Fundamental mode distribution in left and right core at $\lambda = 633$ nm: Pitch $\Lambda = 4.33$ μm , $d_{\text{max}} = 2.6$ μm , $d_{\text{min}} = 0.6$ μm ; all fiber holes are filled with an analyte of refractive index 1.32.

the inclusion of biomolecule layers onto the walls of the holes, as already explained. We only apply this variation on the first ring of air holes around the right core in order to determine the impact on sensitivity of the proposed sensor.

Figure 9 shows the effective refractive index of each mode when the analyte RI changes from 1.32 to 1.44 at $\lambda = 633$ nm. In this figure, we compared the obtained results of the MZI with and without biomolecule layers onto the walls of the holes. From these results, it is clear that in all cases the effective refractive index increases with the analyte RI. As expected, the behavior of the left core is the same in both configurations, due that this core has good confinement fraction and no biomolecule layer. On the other hand, the results of the right core are different, the results with biomolecule layers presents bigger values in the effective refractive index in the whole range, which indicate that the presence of biomolecules can affect the behavior of our configuration. Although the asymmetric nature of the proposed schematic, the chirped MOF-based interferometer is insensitive to the polarization state of the input beam, as we can see from results illustrated in **Figure 9**. This is a great advantage because our sensor does not require controls of polarization. Then, its implementation could be easier than other configurations.

Figure 10(a) shows the effective refractive index difference between the two fundamental modes—for the two orthogonal polarizations and the two studied configurations—that propagate through the fiber cores as a function of analyte RI. Now, from the effective refractive index difference, it is possible to determine the phase difference per unit length, which is given by Eq. (1). In this equation, Δn_{eff} is the effective refractive index difference between the two fundamental modes that propagate through the fiber cores.

$$\delta = \frac{2\pi\Delta n_{\text{eff}}}{\lambda} \quad (1)$$

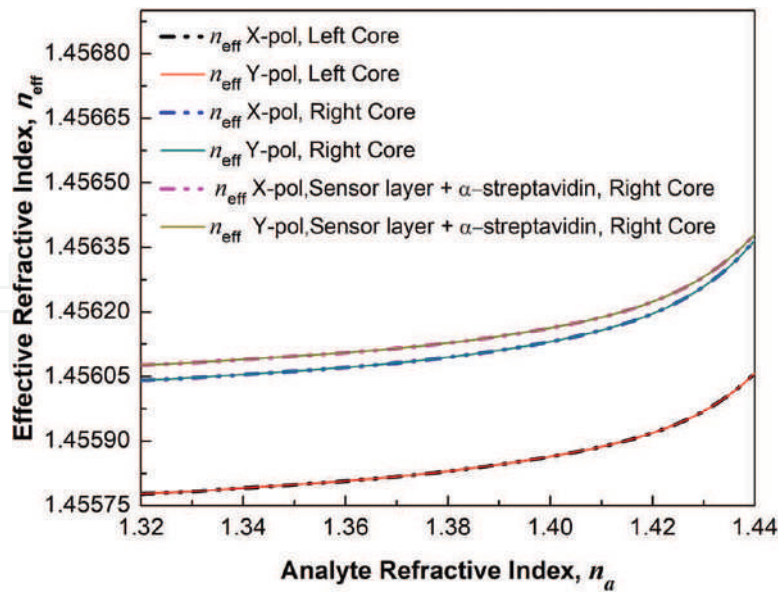


Figure 9. Effective refractive index of the fundamental modes for both polarizations as a function of analyte refractive index. This figure compares obtained results for configurations with and without biomolecules layers.

Figure 10(b) shows the phase difference per unit length as a function of analyte RI. Here, we only present the results for *x*-polarization. As mentioned before, this sensor is polarization-insensitive. As we can see, even though the analyte RI is low, the large differential overlap of the mode cores with the analyte results in a significant amount of phase difference. In both configurations, the phase difference increases exponentially. The configuration with biomolecules layers present higher δ in the whole range compared with the configuration without biomolecule layers. The region from 1.32 to 1.40 presents a phase difference per unit length almost constant in both cases, while for analyte RI higher than 1.40 the phase difference per unit length increases strongly with analyte RI. These results show a better behavior for the

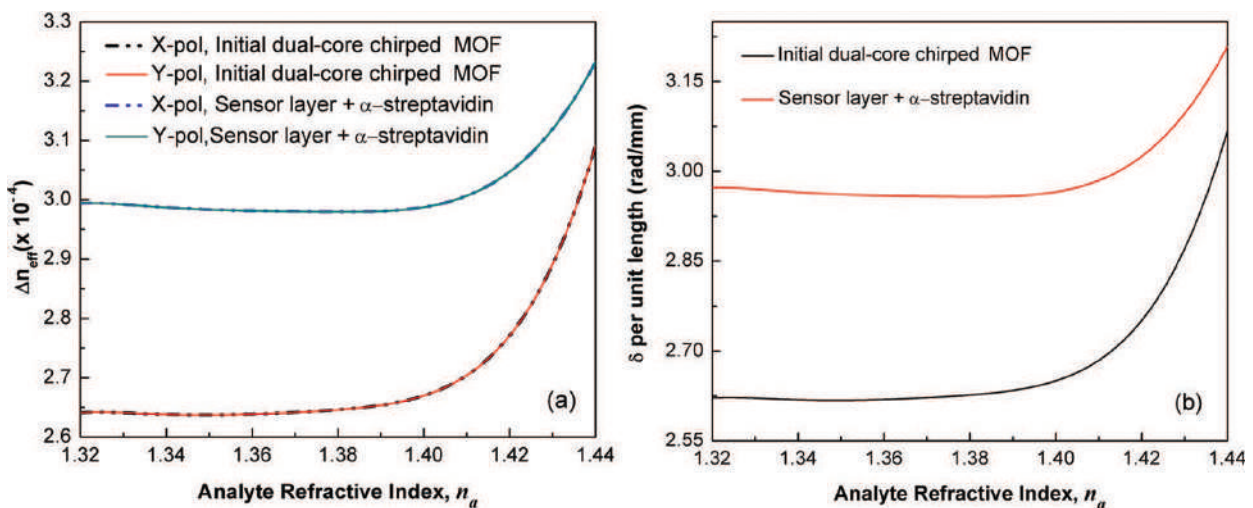


Figure 10. (a) Effective refractive index difference between the two fundamental modes that propagate through the fiber cores as a function of analyte refractive index. (b) Phase difference between the two fundamental modes that propagate through the fiber cores as a function of analyte refractive index (*x*-polarization).

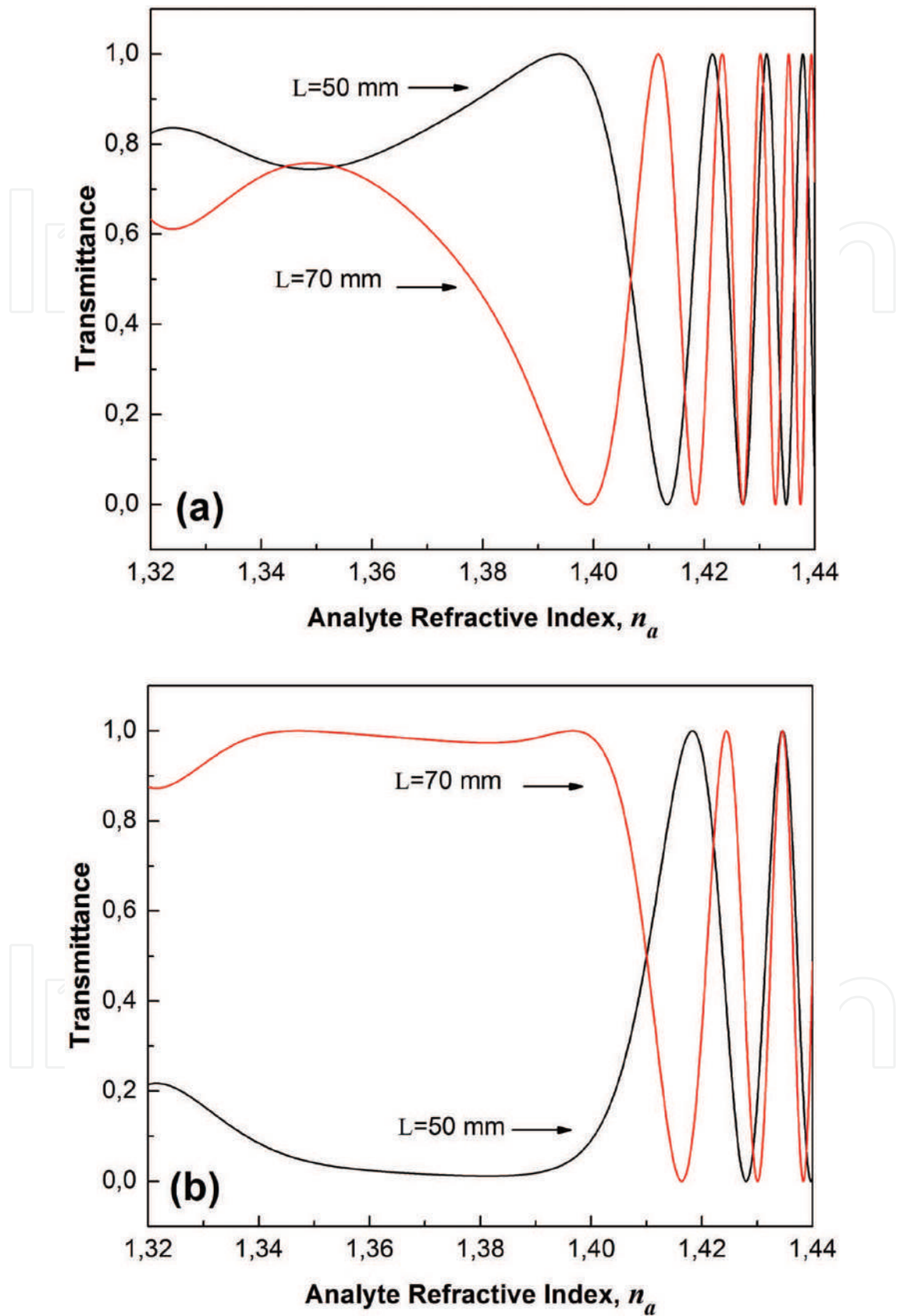


Figure 11. Transmittance of the dual-core transversally chirped MOF for $L = 50$ mm and $L = 70$ mm as a function of analyte refractive index: (a) RI sensor without biomolecules layers; (b) RI sensor with biomolecules layers into the first ring of air holes around the right core.

configuration without biomolecules layers. We believe that it is due to that the layers help to confine the light within the right core.

The phase difference per unit length obtained in **Figure 10(b)** was analytically approximated by an exponential function, which was used to obtain the transmittance of the both sensing configurations. For a balanced interferometer, the normalized transmittance can be calculated by using the following expression

$$T = \cos^2\left(\frac{\delta L}{2}\right) \quad (2)$$

where L is the total length of the sensor. Note that as the analyte refractive index increases, the transmittance passes through a series of nulls and peaks as the phase difference increases. In our case, the fact that the periodic variation of transmittance is reducing indicates that the phase difference between the optical paths of the chirped MOF interferometer changes increasingly rapidly with increasing analyte RI. In addition, these results show that the best region to implement the proposed interferometric schemes is for analyte RI from 1.40 to 1.44.

For best sensitivity, the sensor must be biased to operate at 50% transmittance around a given value of refractive index. In practice, this condition may be achieved by fabricating the device with a length so that $\delta = \pi/2$ (plus any multiple of π radians), or by temperature or wavelength tuning. In **Figure 11(a)**, we can see that the sensitivity of the dual-core transversally chirped MOF structure scales with device length. For example, the sensitivity around $n_a = 1.42$ is $3.028 \times 10^2 \text{ RIU}^{-1}$ for a 70-mm-long device, which gives a detection limit of $3.303 \times 10^{-6} \text{ RIU}$ assuming that we can detect transmittance variations of 10^{-3} . On the other hand, from the **Figure 11(b)** the configuration with biomolecules layers in the first ring of air holes around the right core present a sensitivity equal to $1.83 \times 10^2 \text{ RIU}^{-1}$ around $n_a = 1.42$. In this case, the detection limit is $5.464 \times 10^{-6} \text{ RIU}$. Based on the obtained results, it is clear that the best configuration to measure refractive index changes is the scheme without biomolecules layers. In addition, other works presents the same order of sensitivity [44, 59] but using selective filling of some holes of the microstructure in order to improve the sensor performance.

5. Conclusion

In this chapter, we have presented the concept of dual-core transversally chirped microstructured optical fiber and how this structure can be used in different applications such as mode-converter devices and refractive index sensors. We have shown two simple methods to manufacture this specialty fiber. The effect of pressure inside of fiber holes was demonstrated and the transversal chirp of the MOF can be controlled.

Based on this novel concept, a mode selective coupler was designed and analyzed. We demonstrated a promising platform to manufacture compact and highly efficient mode converters. Through the fluid-filling post-processing technique the operating wavelength and the coupling efficiency can be continuously tuned by varying the temperature. The coupling efficiency over the entire wavelength range between $1.2 \mu\text{m}$ and $1.7 \mu\text{m}$ was greater than 65%.

Consequently, the proposed mode converter can operate in the E + S + C + L + U bands. In general, this kind of mode selective coupler has potential applications in MDM optical fiber communications since it can increase the channel capacity.

Finally, sensing possibilities enabled by the concept of transversally chirped microstructure have been proved, which can be exploited for refractive index sensing in an interferometric arrangement. We have also identified some features of this sensor, including high sensitivity and resolution and scalability of the sensitivity with sensor length. The sensor can be operated over a wide range of analyte refractive index values with a higher sensitivity compared to other selectively filled MOF sensors.

Acknowledgements

This work was supported in part by the Universidad Nacional de Colombia and the Instituto Tecnológico Metropolitano (projects P15108). Erick Reyes-Vera was supported in part by a grant from SPIE.

Author details

Erick Reyes Vera^{1,2*}, Juan Úsuga Restrepo², Margarita Varon¹ and Pedro Torres³

*Address all correspondence to: erickreyes@itm.edu.co

1 Department of Electrical and Electronic Engineering, Universidad Nacional de Colombia, Bogota, Colombia

2 Department of Electronic and Telecommunications, Instituto Tecnológico Metropolitano, Medellín, Colombia

3 Escuela de Física, Universidad Nacional de Colombia, Medellín, Colombia

References

- [1] Richardson DJ, Fini JM, Nelson LE. Space-division multiplexing in optical fibres. *Nature Photonics*. 2013;**7**:354-362
- [2] Tkach RW. Scaling optical communications for the next decade and beyond. *Bell Labs Technical Journal*. 2010;**14**:3-9
- [3] Cai S, Yu S, Lan M, Gao L, Nie S, Gu W. Broadband mode converter based on photonic crystal fiber. *IEEE Photonics Technology Letters*. 2015;**27**:474-477
- [4] Schulze C, Bruning R, Schroter S, Duparre M. Mode coupling in few-mode fibers induced by mechanical stress. *Journal of Lightwave Technology*. 2015;**33**:4488-4496

- [5] Zhang Y, Wang Y, Cai S, Lan M, Yu S, Gu W. Mode converter based on dual-core all-solid photonic bandgap fiber. *Photonics Research*. 2015;**3**:220-223
- [6] Yunhe Zhao, Y. Liu, Jianxiang Wen, and Tingyun Wang, Mode converter based on the long period fiber gratings written in two mode fiber, in 2015 Opto-Electronics and Communications Conference (OECC) (IEEE, 2015), Vol. 24, pp. 1-3
- [7] Martelli P, Gatto A, Boffi P, Martinelli M. Free-space optical transmission with orbital angular momentum division multiplexing. *Electronics Letters*. 2011;**47**:972
- [8] Weng Y, He X, Wang J, Pan Z. All-optical ultrafast wavelength and mode converter based on inter-modal four-wave mixing in few-mode fibers. *Optics Communication*. 2015;**348**:7-12
- [9] Hellwig T, Walbaum T, Fallnich C. Optically induced mode conversion in graded-index fibers using ultra-short laser pulses. *Applied Physics B: Lasers and Optics*. 2013;**112**:499-505
- [10] Shi CX, Okoshi T. Mode conversion based on the periodic coupling by a reflective fiber grating. *Optics Letters*. 1992;**17**:1655-1657
- [11] Usuga J, Amariles D, Correa N, Reyes-Vera E, Gomez-Cardona N. Analysis of chromatic dispersion compensator using a PCF with elliptical holes. *Revista Colombiana de Física*. 2016;**33**:38-41
- [12] Birks TA, Knight JC, Russell PSJ. Endlessly single-mode photonic crystal fiber. *Optics Letters*. 1997;**22**:961
- [13] Ortigosa-Blanch A, Knight JC, Wadsworth WJ, Arriaga J, Mangan BJ, Birks TA, Russell PS. Highly birefringent photonic crystal fibers. *Optics Letters*. 2000;**25**:1325-1327
- [14] Eggleton B, Kerbage C, Westbrook P, Windeler R, Hale A. Microstructured optical fiber devices. *Optics Express*. 2001;**9**:698
- [15] Reyes-Vera E, Gonzalez-Valencia E, Torres P. Understanding the birefringence effects in an all-fiber device based on photonic crystal fibers with integrated electrodes. *Photonics Letters of Poland*. 2010;**2**:168-170
- [16] Reyes-Vera E, Gonzalez-Valencia E, Torres P. Transverse stress response of FBGs in large-mode-area microstructured Panda-type fibers. In: Hernández-Cordero J, Torres-Gómez I, Méndez A, editors. *Proceedings of SPIE*. Vol. 7839. 2010. p. 78391G
- [17] Reyes-Vera E, Torres P. Influence of filler metal on birefringent optical properties of photonic crystal fiber with integrated electrodes. *Journal of Optics*. 2016;**18**:85804
- [18] Khaleque A., Franco MAR, and Hattori H, Ultra-broadband and compact polarization splitter for sensing applications, in *Photonics and Fiber Technology 2016 (ACOFT, BGPP, NP)* (OSA, 2016), Vol. 2, p. JM6A.2
- [19] Franco MAR, Serrão VA, Sircilli F. Microstructured optical fiber for residual dispersion compensation over S+C+L+U Wavelength Bands. *IEEE Photonics Technology Letters*. 2008;**20**:751-753

- [20] Betancur-Pérez AF, Botero-Cadavid JF, Reyes-Vera E, Gómez-Cardona N. Hexagonal photonic crystal fiber behaviour as a chromatic dispersion compensator of a 40 Gbps link. *International Journal of Electronics and Telecommunications*. 2017;**63**:93-98
- [21] Chen MY, Chiang KS. Mode-selective characteristics of an optical fiber with a high-index core and a photonic bandgap cladding. *IEEE Journal of Selected Topics in Quantum Electronics*. 2016;**22**:251-257
- [22] Huang W, Liu Y, Wang Z, Zhang W, Luo M, Liu X, Guo J, Liu B, Lin L. Generation and excitation of different orbital angular momentum states in a tunable microstructure optical fiber. *Optics Express*. 2015;**23**:33741-33752
- [23] Cai S, Yu S, Wang Y, Lan M, Gao L, Gu W. Hybrid dual-core photonic crystal fiber for spatial mode conversion. *IEEE Photonics Technology Letters*. 2016;**28**:339-342
- [24] Reyes Vera EE, Usuga Restrepo JE, Gómez Cardona NE, and Varón M. Mode selective coupler based in a dual-core photonic crystal fiber with non-identical cores for spatial mode conversion, in *Latin America Optics and Photonics Conference (OSA, 2016)*, p. LTu3C.1
- [25] Frazão O, Santos JL, Araújo FM, Ferreira LA. Optical sensing with photonic crystal fibers. *Laser & Photonics Reviews*. 2008;**2**:449-459
- [26] Torres P, Reyes-Vera E, Díez A, Andrés MV. Two-core transversally chirped microstructured optical fiber refractive index sensor. *Optics Letters*. 2014;**39**:1593-1596
- [27] Rindorf L, Bang O. Sensitivity of photonic crystal fiber grating sensors: biosensing, refractive index, strain, and temperature sensing. *Journal of the Optical Society of America B: Optical Physics*. 2008;**25**:310
- [28] Zhang X, Peng W. Fiber Bragg grating inscribed in dual-core photonic crystal fiber. *IEEE Photonics Technology Letters*. 2015;**27**:391-394
- [29] Reyes-Vera E, Cordeiro CMB, Torres P. Highly sensitive temperature sensor using a Sagnac loop interferometer based on a side-hole photonic crystal fiber filled with metal. *Applied Optics*. 2017;**56**:156
- [30] Villatoro J, Minkovich VP, Zubia J. Photonic crystal fiber interferometric force sensor. *IEEE Photonics Technology Letters*. 2015;**27**:1181-1184
- [31] Villatoro J, Minkovich VP, Zubia J. Photonic crystal fiber interferometric vector bending sensor. *Optics Letters*. 2015;**40**:3113
- [32] Osório JH, Hayashi JG, Espinel YAV, Franco MAR, Andrés MV, Cordeiro CMB. Photonic-crystal fiber-based pressure sensor for dual environment monitoring. *Applied Optics*. 2014;**53**(3668)
- [33] Wang J-N, Tang J-L. Photonic crystal fiber Mach-Zehnder interferometer for refractive index sensing. *Sensors (Basel)*. 2012;**12**:2983-2995
- [34] Silva S, Roriz P, Frazão O. Refractive index measurement of liquids based on microstructured optical fibers. *Photonics*. 2014;**1**:516-529

- [35] Oliveira R, Osório JH, Aristilde S, Bilro L, Nogueira RN, Cordeiro CMB. Simultaneous measurement of strain, temperature and refractive index based on multimode interference, fiber tapering and fiber Bragg gratings. *Measurement Science and Technology*. 2016;**27**:75107
- [36] Osório JH, Oliveira R, Aristilde S, Chesini G, Franco MAR, Nogueira RN, Cordeiro CMB. Bragg gratings in surface-core fibers: Refractive index and directional curvature sensing. *Optical Fiber Technology*. 2017;**34**:86-90
- [37] Markos C, Yuan W, Vlachos K, Town GE, Bang O. Label-free biosensing with high sensitivity in dual-core microstructured polymer optical fibers. *Optics Express*. 2011;**19**(7790-8)
- [38] Reyes-Vera E, Gómez-Cardona N, Torres P. Label-free biosensor based on a dual-core transversally chirped microstructured optical fiber. In: López-Higuera JM, Jones JDC, López-Amo M, Santos JL, editors. *Proceedings of SPIE*. Vol. 9157. 2014 91578J
- [39] Monro TM, Belardi W, Furusawa K, Baggett JC, Broderick NGR, Richardson DJ. Sensing with microstructured optical fibres. *Measurement Science and Technology*. 2001;**12**: 854-858
- [40] Mägi E, Steinvurzel P, Eggleton B. Tapered photonic crystal fibers. *Optics Express*. 2004;**12**(776-84)
- [41] Velasquez-Botero F, Reyes-Vera E, Torres P. Some refractometric features of dual-core chirped microstructured optical fibers. In: Kalinowski HJ, Fabris JL, Bock WJ, editors. *Proceedings of SPIE*. Vol. 9634. 2015 963450
- [42] Wu DKC, Kuhlmeiy BT, Eggleton BJ. Ultrasensitive photonic crystal fiber refractive index sensor. *Optics Letters*. 2009;**34**:322
- [43] Kuhlmeiy BT, Coen S, Mahmoodian S. Coated photonic bandgap fibres for low-index sensing applications: cutoff analysis. *Optics Express*. 2009;**17**:16306-16321
- [44] Sun B, Chen M-Y, Zhang Y-K, Yang J-C, Yao J, Cui H-X. Microstructured-core photonic-crystal fiber for ultra-sensitive refractive index sensing. *Optics Express*. 2011;**19**(4091-4100)
- [45] Matuschek N, Kartner FX, Keller U. Analytical design of double-chirped mirrors with custom-tailored dispersion characteristics. *IEEE Journal of Quantum Electronics*. 1999;**35**:129-137
- [46] Riant I, Gurib S, Gourhant J, Sansonetti P, Bungarzeanu C, Kashyap R. Chirped fiber Bragg gratings for WDM chromatic dispersion compensation in multispan 10-Gb/s transmission. *IEEE Journal of Selected Topics in Quantum Electronics*. 1999;**5**:1312-1324
- [47] Skibina JS, Iliew R, Bethge J, Bock M, Fischer D, Beloglasov VI, Wedell R, Steinmeyer G. A chirped photonic-crystal fibre. *Nature Photonics*. 2008;**2**:679-683

- [48] Ghosh S, Varshney RK, Pal BP, Monnom G. A Bragg-like chirped clad all-solid micro-structured optical fiber with ultra-wide bandwidth for short pulse delivery and pulse reshaping. *Optical and Quantum Electronics*. 2010;**42**:1-14
- [49] Russell PSJ. Photonic-crystal fibers. *Journal of Lightwave Technology*. 2006;**24**:4729-4749
- [50] Méndez A, Morse TF. *Specialty Optical Fibers Handbook*. London, Academic Press; 2007
- [51] Bansal NP. *Handbook of Glass Properties*. London, Academic Press; 1986
- [52] Du F, Lu Y-Q, Wu S-T. Electrically tunable liquid-crystal photonic crystal fiber. *Applied Physics Letters*. 2004;**85**:2181-2183
- [53] Larsen T, Bjarklev A, Hermann D, Broeng J. Optical devices based on liquid crystal photonic bandgap fibres. *Optics Express*. 2003;**11**(2589-96)
- [54] Alkeskjold TT, Lægsgaard J, Bjarklev A, Hermann DS, Anawati A, Broeng J, Li J, Wu S-T. All-optical modulation in dye-doped nematic liquid crystal photonic bandgap fibers. *Optics Express*. 2004;**12**:5857
- [55] Steinvurzel P, Eggleton BJ, de Sterke CM, Steel MJ. Continuously tunable bandpass filtering using high-index inclusion microstructured optical fibre. *Electronics Letters* 2005;**41**:463
- [56] Alkeskjold TT, Bjarklev A. Electrically controlled broadband liquid crystal photonic bandgap fiber polarimeter. *Optics Letters*. 2007;**32**:1707
- [57] Snyder AW, Love JD. *Optical Waveguide Theory*. New York, Springer US; 1983
- [58] Lee DL. *Electromagnetic Principles of Integrated Optics*. 1st ed. New Jersey, Wiley; 1986
- [59] Wu Y, Town GE, Bang O. Refractive index sensing in an all-solid twin-core photonic bandgap fiber. *IEEE Sensors Journal*. 2010;**10**:1192-1199

IntechOpen